



Sichuan University - Pittsburgh Institute



UNDERGRADUATE SENIOR PROJECT REPORT

High Performance Heat Exchanger Design Based on Bionic Structures

by

Litao Liu (Team Leader)

Junce Pu

Ao Qi

Xingyi Li

Sichuan University - Pittsburgh Institute

2023

Copyright in this work rests with the authors. Please ensure that any reproduction or re-use is done in accordance with the relevant national copyright legislation.

Declarations

Project Team Members

Role	Student Name	Student ID	Major
Team Leader	Litao Liu	2019141520065	ME
Team Member	Junce Pu	2019141520045	ME
Team Member	Ao Qi	2019141520002	ME
Team Member	Xingyi Li	2019141520097	ME

Advisory Committee Members

	Name	Department/Affiliation
Advisor	Minking Chyu	Professor
Co-Advisor	Dong Liang	Doctor
Outside major faculty		
Non-tech Major faculty		

Abstract

Heat exchangers (HX) have a wide range of applications in various fields, such as industrial production and aerospace. The rapid development of additive manufacturing (AM) in recent years has made it possible to produce HXs with complex internal structures. Among these, the HX with triply periodic minimal surface (TPMS) structures has drawn the attention of many researchers due to its large area-to-volume ratio, flexible design capabilities, and the feature of separating hot and cold flow channels. It has been believed to have the potential to replace traditional plate and tube HXs and revolutionize the entire field of HX design. TPMS is a specific type of three-dimensional surface with certain mathematical formula, and is suitable for constructing high performance HX. Among the TPMS structures, the F-RD topology shows good mechanical properties, while the flow characteristics and mechanism inside F-RD HX have not been clarified yet. Therefore, this study reports the design and fabrication of an F-RD aluminum HX via AM. By conducting numerical simulations and heat transfer experiments, the internal flow characteristics and heat transfer performance of the F-RD HX are analyzed. Based on the literature review, the S-D topology exhibits the best heat transfer performance among TPMS structures. This research findings show that the F-RD topology demonstrates comparable heat transfer performance in contrast with the S-D topology. However, due to the different blockage areas, the F-RD HX exhibits different pressure drops in hot the and cold channels, which are larger than those of the S-D HX. These characteristics allow F-RD HXs to be the suitable option for scenarios that require both good mechanical and heat transfer performance. In addition, to improve the design flexibility of HXs and adapt to a wider range of application scenarios, this study also explores the modeling method of Hybrid-TPMS structure. The findings of this study will provide valuable insights for the optimal design of HXs.

Keywords: Heat Exchanger; Triply Periodic Minimal Surface; Additive Manufacturing; Numerical Simulation; Hybrid-TPMS.

Table of Contents

Declarations.....	ii
Abstract	iii
Table of Contents	iv
List of Tables	vi
List of Figures	vii
List of Acronyms	ix
Glossary	x
Chapter 1. Introduction.....	1
Chapter 2. Technical Background.....	1
2.1. Triply Periodic Minimal Surface (TPMS) Structure	1
2.2. Computational Fluid Dynamics (CFD) Technology	2
2.3. Hybrid-TPMS (H-TPMS) Structure	4
2.4. Additive Manufacturing (AM) Technology.....	5
Chapter 3. Heat Exchanger Design and Manufacture.....	8
3.1. Heat Exchanger Design	8
3.2. Manufacturability Evaluation	9
3.2.1. Dimensional Accuracy.....	10
3.2.2. Surface Morphology	11
3.2.3. Defect Observation.....	13
Chapter 4. Numerical Simulation of Heat Transfer Process	15
4.1. Numerical Simulation Model Design	15
4.2. Meshing of Computational Domain	16
4.3. Ansys-CFX Pre-processing.....	18
4.4. Numerical Simulation Verification	19
4.5. Analysis of Numerical Simulation Results	22
4.6. Summary of Numerical Simulation	29
Chapter 5. Heat Transfer Experiment	31
5.1. Heat Transfer Experimental Design	31
5.2. Data Extraction.....	33
5.3. Uncertainty Analysis.....	36
5.4. Analyzing Experimental Results	38
5.5. Summary of Experiment	43
Chapter 6. Mechanical Compression Test	44
Chapter 7. Exploration of Hybrid-TPMS Structure	46
7.1. Uniform TPMS Structure Modeling	46
7.1.1. Characteristic Curves	47
7.1.2. Parameter Surface	48

7.1.3. Sandwich Structure Modeling	49
7.2. H-TPMS Structure: L-CTG modeling	49
Chapter 8. Conclusion and Future Works	52
8.1. Conclusion.....	52
8.2. Future Works	53
References	55
Appendix A. H-TPMS Modeling Code	58

List of Tables

Table 2.1.	Mathematical expressions of different TPMS units.	1
Table 3.1.	The design details of F-RD HX.	8
Table 3.2.	Parameters of the F-RD array....	10
Table 4.1.	Simulation model design details.	15
Table 4.2.	Grid independence check results for the F-RD HX.	18
Table 6.1.	Statistics of mechanical properties.	45

List of Figures

Figure 1.1.	The core contents of this project.....	2
Figure 2.1.	The general steps in fluid numerical calculation (See Chapter 4 for details).....	3
Figure 2.2.	Some hybrid forms, (a) relative density grading (RDG), (b) cell size grading (CSG), (c) circular cell type grading (C-CTG), (d) linear cell type grading (L-CTG).	5
Figure 2.3.	(a)SLM printer (source: https://www.51sole.com/xinxi/128967841.htm), (b) SLM prints schematics (source: https://www.researchgate.net/figure/Schematic-of-the-SLM-process_fig2_334230008).....	6
Figure 3.1.	F-RD HX models of interest in this study (a) F-RD unit, (b) 3x3x3 array of F-RD unit, (c) Cross-section of the overall HX.	8
Figure 3.2.	Manufactured products, (a) F-RD array, (b)F-RD HX.	9
Figure 3.3.	Picture of scanning electron microscope experiment machine.	10
Figure 3.4.	Wall thickness selection example.	11
Figure 3.5.	Building direction of F-RD array.....	12
Figure 3.6.	SEM pictures at (a) Top of F-RD array, (b) Bottom of F-RD array, (c) height map of top surface (500x), (d) height map of bottom surface (500x).	12
Figure 3.7.	(a) Definition of Ra, (b) Definition of Rz.	13
Figure 4.1.	The 3x3x1 TPMS unit array models of numerical simulation (a) F-RD HX, (b) S-D HX.....	16
Figure 4.2.	Numerical simulation model meshing steps.	17
Figure 4.3.	Mesh detail of a section inside the S-D HX.	18
Figure 4.4.	Comparison of overall heat transfer coefficient U between simulation and experiment, (a) U vs Re, (b) U under the hot flow with a velocity of 1 m/s.....	21
Figure 4.5.	Comparison of heat transfer effectiveness ε between simulation and experiment, (a) numerical simulation results, (b) experimental results.	21
Figure 4.6.	Fluid temperature distribution in the internal section of the HX, (a) F-RD HX, (b) S-D HX.....	23
Figure 4.7.	Velocity streamline of the heat flow inside the HX, (a) F-RD HX, (b) S-D HX.	24
Figure 4.8.	The velocity distribution of the internal section of the HX along the y-axis, (a) F-RD HX, (b) S-D HX.	25
Figure 4.9.	Temperature profile of the solid region of the HXs, (a) F-RD HX, (b) S-D HX.	26
Figure 4.10.	Heat flux on the solid surface of HX cores, (a) F-RD HX, (b) S-D HX.	27
Figure 4.11.	The core detail of the numerical simulation models, (a) F-RD HX, (b) S-D HX.....	28
Figure 5.1.	Experimental setup, (a) The overall diagram of the experimental pipeline, (b) Air compressor, (c) Air dryer.....	31
Figure 5.2.	The assembly details of the experimental pipeline and HX, (a) experimental system, (b) Schematic diagram of the heat transfer experiment.	32
Figure 5.3.	Correction factor for a single-pass, cross-flow heat exchanger with both fluids unmixed (Whitaker 2013).	35
Figure 5.4.	Results of the average heat exchange rate experiments, (a) Q_avg(1:1) versus Re, (b) Q_avg(2:1) versus Re.....	38

Figure 5.5.	Results of the heat transfer efficiency experiments, (a) Effectiveness(1:1) versus Re, (b) Effectiveness(2:1) versus Re, (c) Effectiveness(1:1) versus NTU, (d) Effectiveness(2:1) versus NTU.	39
Figure 5.6.	Results of the heat transfer coefficient experiments, (a) U(1:1) versus Re, (b) U(2:1) versus Re, (c) U*A(1:1) versus Re, (d) U*A(2:1) versus Re.	40
Figure 5.7.	Results of the Nusselt number experiment, (a) Nu(1:1) versus Re, (b) Nu(2:1) versus Re.	41
Figure 5.8.	Results of pressure drop experiments, (a) pressure drop(1:1) versus Re, (b) pressure drop(2:1) versus Re.	41
Figure 5.9.	Results of friction coefficient experiments, (a) resistance coefficient(1:1) versus Re, (b) resistance coefficient(2:1) versus Re	42
Figure 5.10.	Results of overall thermal efficiency experiments, comprehensive heat transfer coefficients (1:1) versus Re.	43
Figure 6.1.	Mechanical compression test equipment.	44
Figure 6.2.	Compression test curve.	45
Figure 7.1.	Workflow chart for L-CTG H-TPMS modeling.	46
Figure 7.2.	Pont cloud models, (a)Point cloud model of S-D before denoising, (b)Point Cloud Model of S-D after denoising.	47
Figure 7.3.	(a) Sum model of characteristic curves for S-D, (b) Surface model of S-D, (c) Sheet-Work S-D structure.	48
Figure 7.4.	(a) Point cloud for S-D in D1, (b) Parameter surface for S-D in D1, (c) Parameter surface for S-D structure.	48
Figure 7.5.	(a) Surface for fS-D = 0.2, (b) Surface for fS-D = 0.2, (c) Sandwich Sheet-Work structure for S-D.	49
Figure 7.6.	(a) Characteristic curves of Transition of Gyroid to S-D, (b) Surface of Transition of Gyroid to S-D, (c) Solid-Work for L-CTG structure between Gyroid and S-D in domain D.	50
Figure 7.7.	Truss-Work for L-CTG structure between Gyroid and S-D in domain D2.....	51
Figure 7.8.	(a) Surface FS-D&Gyroid = 0.2, (b) Surface FS-D&Gyroid = -0.2, (c) Sandwich expression for L-CTG, (d) Sheet-Work for L-CTG structure between G and S-D.	51

List of Acronyms

AM	Additive manufacturing
CSG	Cell size grading, a kind of H-TPMS
C-CTG	Circular cell type grading, a kind of H-TPMS
CFD	Computational fluid dynamics
CAD	Computer aided design
G	Gyroid, the name of a TPMS topology
TPMS	Triply periodic minimal surface
HX	Heat exchanger
HXs	Heat exchangers
H-TPMS	Hybrid triply periodic minimal surface
L-CTG	Linear cell type grading, a kind of H-TPMS
NTU	Number of transfer units
P	Primitive, the name of a TPMS topology
RDG	Relative density grading, a kind of H-TPMS
SEM	Scanning electron microscopy
S-D	Schwarz-D, the name of a TPMS topology
SLM	Selective laser melting

Glossary

Additive manufacturing	A new type of manufacturing process. Complicated structures can be processed.
Array	A periodic arrangement of unit cells in a specific direction.
Baffle area	The sealing area of the outermost layer of the internal array of the heat exchanger.
Channel	The domain through which hot and cold flows flow.
Computational Fluid Dynamics	Computational Fluid Dynamics is an interdisciplinary science with remarkable vitality that emerged from the fusion of modern fluid mechanics, numerical mathematics, and computer science.
Friction coefficient (f)	Friction coefficient (f) is a parameter that describes the level of frictional resistance between a fluid and a solid surface. It is an important factor that affects the convective heat transfer coefficient and the overall heat transfer rate in a system.
Heat exchanger	A device used to transfer heat between hot and cold fluids.
Heat transfer effectiveness (ε)	Heat transfer effectiveness (ε) is a measure of how effectively heat is transferred from one fluid to another or from a solid surface to a fluid. It is a dimensionless quantity that compares the actual heat transfer rate to the maximum possible heat transfer rate between the two fluids or between the solid surface and the fluid.
Heat transfer rate (Q)	Heat transfer rate (Q) refers to the amount of heat transferred per unit time. It is a measure of the rate at which heat is transferred from one body or system to another, and is typically expressed in units of watts (W) or British thermal units per hour (BTU/hr).
Hydraulic diameter (D_h)	Hydraulic diameter (D_h) is a parameter used in fluid mechanics to characterize the flow of fluid through a pipe. It is a measure of the effective diameter of the duct or pipe, taking into account both its actual physical dimensions and its shape.
Logarithmic mean temperature difference ($LMTD$)	Logarithmic mean temperature difference ($LMTD$) is a measure used in heat transfer calculations to determine the temperature driving force for heat transfer in a heat exchanger.
Mass flow rate (\dot{m})	Mass flow rate (\dot{m}) is the amount of mass passing through a given cross-sectional area per unit time. It is a measure of the rate at which mass is transferred, and is typically expressed in units of kilograms per second (kg/s) or pounds per minute (lb/min).
Maximum height of the profile (Rz)	Maximum height of the profile (Rz) is the distance between the peak line and the bottom line of the profile, which is an indicator used to measure surface roughness.
Number of transfer units (NTU)	Number of transfer units (NTU) is a dimensionless parameter commonly used in heat exchanger design and analysis. It represents the ratio of the heat transfer surface area to the

	characteristic length scale of the flow path, and is a measure of the effectiveness of the heat exchanger.
Nusselt number (Nu)	Nusselt number (Nu) is a dimensionless parameter used in heat transfer analysis to describe the convective heat transfer coefficient between a fluid and a solid surface.
Overall heat transfer coefficient (U)	Overall heat transfer coefficient (U), is a measure of the overall rate of heat transfer across a surface or a boundary between two fluids. Typically, heat exchangers with larger U values are more favored.
Overall thermal efficiency (η)	Overall thermal efficiency (η) is a measure of the efficiency of a thermal system that converts heat into useful work or other forms of energy. It is defined as the ratio of the useful output of the system to the input energy in the form of heat.
Porosity	The ratio of the difference between the cube of the side length and the cell volume to the cube of the side length.
Pressure drop (ΔP)	Pressure drop (ΔP) is the decrease in pressure that occurs as a fluid flows through a system, such as a pipe. It is a measure of the resistance to flow in a system, and is typically expressed in units of pressure, such as pounds per square inch (psi) or pascals (Pa).
Profile arithmetic mean deviation (Ra)	Profile Arithmetic Mean Deviation (Ra) is the arithmetic mean of the absolute value of the measured object's internal contour offset, which is used in this study to evaluate the surface roughness of the research object.
Reynolds Number (Re)	Reynolds number (Re) is a dimensionless quantity used in fluid mechanics to characterize the behavior of fluid flow in different situations. The Reynolds number helps to predict the onset of turbulence in a fluid flow. When the Reynolds number is below a certain critical value, the flow is laminar, meaning that it is smooth and predictable. When the Reynolds number exceeds the critical value, the flow becomes turbulent, characterized by chaotic, swirling motion and mixing of the fluid.
Selective laser melting	One of the additive manufacturing technologies.
Specific heat (C_p)	Specific heat (C_p) is the amount of heat energy required to raise the temperature of one unit of mass of a substance by one degree Celsius (or one Kelvin). It is a material property that measures the amount of thermal energy required to cause a temperature change in a given substance.
Thermal conductivity (K)	Thermal conductivity (K) is the ability of a material to conduct heat. It is a measure of the rate at which heat energy is transferred through a material due to a temperature difference between two points.
Volume-based power density ($VBPD$)	Volume-based power density is a measure of the amount of power that can be transferred per unit volume of a device or system.

Chapter 1.

Introduction

A heat exchanger (HX) is a mechanical device used to transfer heat from a hot flow to a cold flow. HXs are widely used in aerospace, automotive, electronics, food production, natural gas and other industrial fields (Mekki, Langer, and Lynch 2021; Zhao, Wang, and Ge 2021; Bai et al. 2021; Xie et al. 2022; Elsheikh et al. 2022). The findings of Ahmadi and Bigham show that the material and internal structure are the main factors affecting the heat transfer performance of the HX (Ahmadi and Bigham 2022). In the past, HXs with simple internal structures, such as tube and plate types, were commonly used. In recent years, to pursue superior heat transfer performance, researchers attempted to design HXs with more complex internal structures. Fortunately, with the rapid development of additive manufacturing (AM), it becomes possible to fabricate these complex HXs for practical heat transfer applications. The primary feature of these HXs is the ability to achieve intricate flow patterns through complex flow channels, resulting in enhanced heat transfer between hot and cold fluids. This development is particularly significant for industries where HXs play a crucial role, such as the chemical, energy, and manufacturing sectors. The combination of complex internal structures and AM has the potential to revolutionize HX design and performance.

In recent years, the rapid development of AM has enabled itself to penetrate many fields and produce subversive reforms, such as pharmaceutical manufacturing, electrical parts processing and robotic parts manufacturing (Kumar et al. 2021; Redondo and Pumera 2021; Delda et al. 2021). The positive change that AM technology will bring to the HX design and production fields is to provide a solution for manufacturing HXs with any complex internal structure. For example, Ahmadi and Bigham designed a bionic HX model based on the inspiration of the lung, produced the HX based on stereo lithography appearance technology, and proved its heat transfer performance is comparable to metal ones through comparative experiments (Ahmadi and Bigham 2022). In recent years, HXs with triply periodic minimal surface (TPMS) structures have garnered significant research attention due to their large area-to-volume ratio, flexible designability, and the feature of separating hot and cold flow channels. Meanwhile, the relatively intricate flow channels inside TPMS structure induces complex flow mechanism that enhances the heat exchange capacity. The TPMS structure is a class of bionic structure, which encompasses several different topologies, such as Primitive (P), Gyroid (G), Schwarz-D (S-D) and F-RD types. For instance, Kim et al. were the first to design a HX with a

TPMS structure and demonstrated that its heat transfer performance surpasses that of a traditional plate-and-frame HX (Kim and Yoo 2020). Subsequently, Liang et al. utilized selective laser melting (SLM) technology to manufacture HXs with various TPMS types and evaluated their heat transfer performance through numerical simulation and experiments. They found that the S-D type had the most excellent heat transfer performance (Liang et al. 2023). These research results represent a significant step forward in the development of HX technology and demonstrates the potential for AM and bionic structure to revolutionize the design and performance of HXs.

Project Content

Design and manufacture HX with F-RD

Investigate flow mechanism through numerical simulation

Analyze heat transfer performance via experiment and compare with S-D HX

Explore the modeling method of Hybrid-TPMS (H-TPMS)

Figure 1.1. *The core contents of this project.*

This research aims to explore the F-RD structure for HX design, building on previous research efforts (Liang et al. 2023). F-RD has been experimentally confirmed to possess good mechanical properties among TPMS structures (Kapfer et al. 2011). However, the flow characteristics and mechanism inside F-RD HX have not been clarified yet. Therefore, the main contribution of this study is investigating the heat transfer performance and mechanism of the F-RD HX through experiments and numerical simulation. To enhance the adjustability of the TPMS HXs, this project will explore the design and optimization of the Hybrid-TPMS structure, which allows TPMS to be applied to more scenarios, such as a curved outer frame (Kim and Yoo 2020). As depicted in Figure 1.1, the main contents of this project include the design and fabrication of F-RD HXs, the investigation of flow mechanism via numerical simulation, assessment of flow and heat transfer performance via experiments, and the modeling methodology of the H-TPMS design. Additionally, scanning electron

microscopy (SEM) is employed to evaluate the manufacturability of additively manufactured HXs. All in all, this study provides a guidance for the development and optimal design of TPMS HXs.

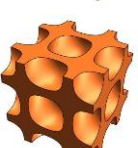
Chapter 2.

Technical Background

2.1. Triply Periodic Minimal Surface (TPMS) Structure

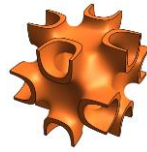
In nature, there are a vast array of porous structures, such as honeycomb, sponge, bone and wood. These structures exhibit outstanding performance in various fields, such as mechanics, heat transfer, and biomedical (Wu, Yang, and Kitipornchai 2020; Cheng, Xu, and Jiang 2021; Lu et al. 2020). Based on the inspiration of nature, scientists have tried to construct some porous bionic structures. At the beginning of the 20th century, scientists proposed a kind of structure that could be expressed by mathematical expressions, which was called triply periodic minimal surface (TPMS) (Lee, Khan, and Al-Rub 2017; Yang et al. 2018; Yeo, Oh, and Yoo 2019). Table 2.1 illustrates some TPMS mathematical equations and their respective unit models. Two critical parameters that affect TPMS are ω and C , which influence period and curvature. Feng et al. studied the models when ω and C take different values. The results show that by changing the values of ω and C , a TPMS structure with a specific desired density can be obtained (Liu et al. 2018; Feng et al. 2021). TPMS structure possess several characteristics, for instance, their high symmetry makes their average curvature equal to 0, the topologies designed based on them is controllable, and they have large surface area to volume ratio (Feng et al. 2018).

Table 2.1. Mathematical expressions of different TPMS units.

Unit name	Mathematical expression	Units
Primitive (P)	$f(x, y, z) = \cos(w_x x) + \cos(w_y y) + \cos(w_z z) = C$	
Gyroid (G)	$f(x, y, z) = \sin(w_x x) \cos(w_y y) + \sin(w_z z) \cos(w_x x) + \sin(w_y y) \cos(w_z z) = C$	
Schwarz-D (S-D)	$f(x, y, z) = \cos(w_x x) \cos(w_y y) \cos(w_z z) - \sin(w_x x) \sin(w_y y) \sin(w_z z) = C$	

F-RD

$$f(x, y, z) = 8 \cos(\omega_x x) \cos(\omega_y y) \cos(\omega_z z) + 3[\cos(\omega_x x) + \cos(\omega_y y) + \cos(\omega_z z)] = C$$



Due to the complex structure of TPMS, the traditional manufacturing process limits its transition from design to application. Fortunately, with the recent rapid advancement of AM, TPMS structures can now be produced and have gained significant attention in various fields. For instance, TPMS structures have demonstrated superior properties in the aviation industry, where the design of aircraft requires a high volume of sandwich panels. Alashaer et al. conducted a study comparing the mechanical properties of traditional sandwich panels and TPMS structural core materials, revealing that TPMS core materials exhibit superior strength and stiffness-to-weight ratio (Alshaer and Harland 2021). In terms of bio-medical engineering, Melchels et al. affirmed the feasibility and effectiveness of TPMS structures as bone defect fillers (Melchels et al. 2010). Lei et al. used the TPMS structure as a catalyst carrier to compare with the current commercial hydrogen production technology. The research shows that the hydrogen production performance can be improved (Lei et al. 2019).

In terms of heat transfer, TPMS structures improve heat transfer performance through large heat transfer areas and complex flow mechanisms, which makes TPMS structures widely discussed in the field of HX design in recent years. For instance, Kim et al. designed and manufactured a HX with TPMS structure for the first time, and proved that its heat transfer performance was better than traditional plate-frame HXs (Kim and Yoo 2020). Reynolds et al. conducted a comparative study of HXs using nine different TPMS single structures and affirmed the superiority of the gyroid TPMS HX over other TPMS structures based on the Nusselt number (Reynolds et al.). Li et al. investigated the superior performance of TPMS HXs by comparing the heat exchange performance of TPMS HXs with printed circuit HXs (Li, Li, and Yu 2022). Liang et al. printed P, G, and S-D type HXs made of aluminum through selective laser melting (SLM) and evaluated three TPMS HXs through simulation and experiments and concluded that S-D type had the best overall performance (Liang et al. 2023). This research will conduct comparative experiments and simulation analysis on the aluminum F-RD HX and explore the modeling methodology of Hybrid-TPMS (H-TPMS), which integrates multiple TPMS unit cells in a single HX.

2. 2. Computational Fluid Dynamics (CFD) Technology

Computational Fluid Dynamics (CFD) is an interdisciplinary science with remarkable vitality that emerged from the fusion of modern fluid mechanics, numerical mathematics, and computer

science. It involves approximating the integral and differential terms in the governing equations of fluid mechanics into discrete algebraic forms, resulting in a system of algebraic equations that can be solved through a computer to obtain numerical values at discrete time or space points. By using CFD, designers can significantly improve design efficiency, and conduct theory-based simulation experiments to predict experimental results, or as one of the basis for verifying the correctness of experimental data (Norton and Sun 2006; Liu and Liu 2021).

Among them, the current mainstream CFD software includes ANSYS-Fluent, ANSYS-CFX, STAR-CCM+, etc., all of which have their own advantages and markets. In this research, the Ansys-CFX software will be used to perform numerical simulation of the F-RD HX. For a CFD calculation example, it is often necessary to include the steps illustrated in Figure 2.1 (Liang et al. 2023; Bajic 2019).

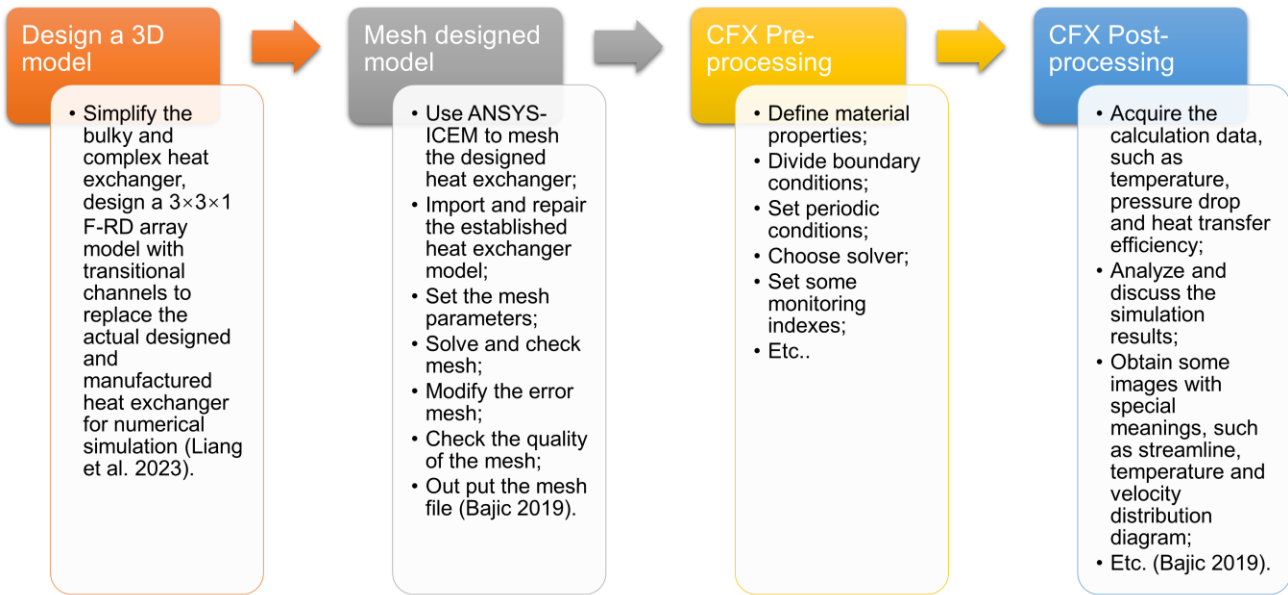


Figure 2.1. The general steps in fluid numerical calculation (See Chapter 4 for details).

Particularly, CFX is a preferred tool for HX design. Li et al. conduct a numerical study on two TPMS HXs and a reference printed circuit HX using the CFX software, which demonstrates that the TPMS HX can improve overall heat transfer performance by 15-100% compared to PCHE (Li, Yu, and Yu 2020). Agarwal performs a numerical analysis of a plate HX using CFX (Agarwal 2021). In the same year, Padmanabhan et al. analyze the heat transfer effect of a spiral-inserted double-tube HX with the assistance of CFX (Padmanabhan et al. 2021). Lesmana and Aziz monitor the pressure

drop and heat transfer performance of the TPMS simulation model through CFX numerical analysis (Lesmana and Aziz 2022). Li and Liang include the CFX numerical simulation part in their comparative experiments on TPMS heat transfer devices, and numerical simulation results assist in the interpretation of experimental results (Li, Li, and Yu 2022; Liang et al. 2023). In this research, the flow characteristics and heat transfer mechanism of the F-RD HX will be explored through CFX numerical simulation.

2.3. Hybrid-TPMS (H-TPMS) Structure

H-TPMS structure corresponds to functionally graded TPMS structures. Alketan et al. introduce three H-TPMS structures, which are Relative density grading (RDG), Unit cell size grading (UCSG), Cell type grading (CTG) (AI - Ketan and Abu AI - Rub 2021) Particularly, two different paths of CTG are listed: circular transition cell type grading (C-CTG) and linear transition Cell type grading (L-CTG). Figure 2.2 (a) shows the RDG G model, in which the model's wall thickness decreases as height grows. Figure 2.2 (b) shows the UCSG G model and model's cell size decreases when height increases. Figure 2.2 (c) shows C-CTG of G and S-D with transition taking place at the surface $x^2 + y^2 = r^2$. Figure 2.2 (d) shows L-CTG of G and S-D and transition takes place at the surface $x = 0$.

Wang et al. investigate 3 different RDG P model: *Uniform unit cell P* model with a porosity of 0.56, *Normal RDG P* model with a maximum porosity of 0.735 varying from top to bottom with the gradient ranging from 1100 μm to 500 μm and *Symmetric RDG P* model with maximum porosity of 0.735, which is the centrally symmetric version of *Normal RDG P* model. The results show that as bone tissue replacement the mechanical properties and permeability of the designed original surface scaffold have good effects (Wang et al. 2020). Among them, *Symmetric RDG P* model's potential in artificial bone scaffolds is noticeable, while *Uniform unit cell P* model's potential leads to its better mechanical properties. Zhang Xinyue studies the Sheet-Work model of UCSG TPMS S-D with different cell sizes (Zhang 2019). Through the compression test, it is found that the energy absorption capacity and compressive strength of the model decreased with the increase of cell size.

The CTG H-TPMS structure hybridizes different TPMS structures. The CTG H-TPMS structure can be used under complex conditions of HXs. For an example, a load concentration happens in part of an S-D HX and causes a collapse. F-RD structure approximately withstands this load concentration. Replacing this S-D part by F-RD helps this HX's resurrection. Meantime, CTG H-TPMS can hybridize S-D and F-RD. Therefore, it is worthy to study H-TPMS structure. Meanwhile, L-CTG model between G and S-D is chosen to explore the modeling methodology.

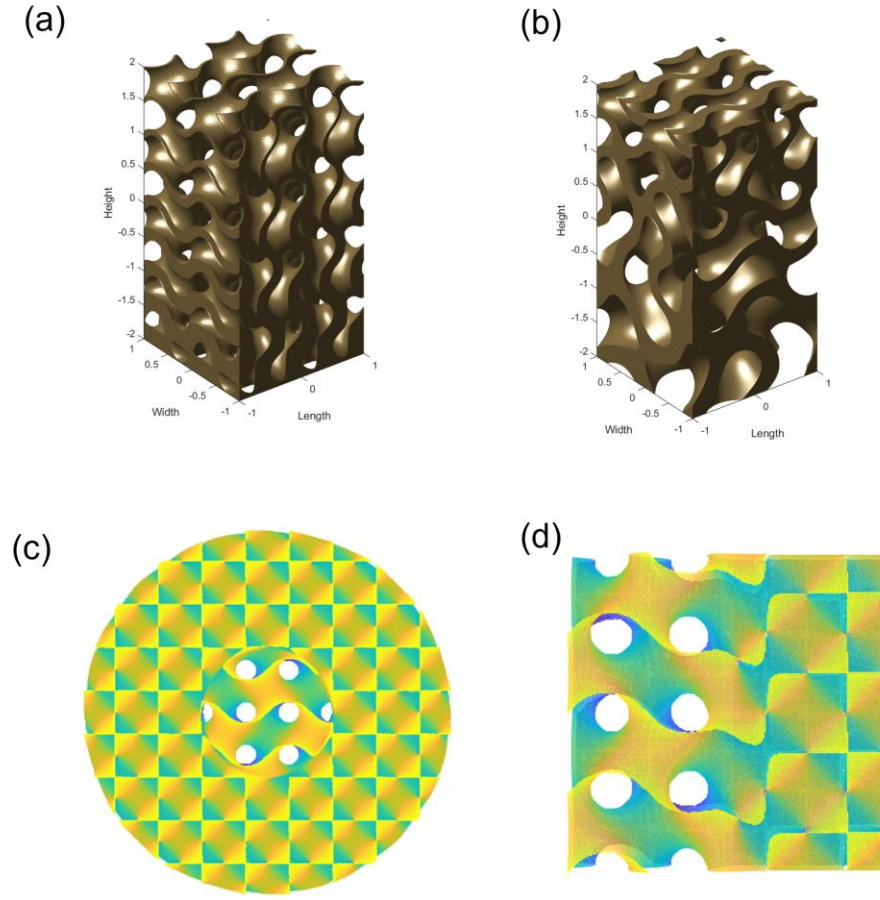


Figure 2.2. Some hybrid forms, (a) relative density grading (RDG), (b) cell size grading (CSG), (c) circular cell type grading (C-CTG), (d) linear cell type grading (L-CTG).

2.4. Additive Manufacturing (AM) Technology

AM is an efficient, simple, high completion of the processing method, which accumulate of raw materials to produce products. Compared with the subtractive manufacturing (SM) technology, AM technology does not need the traditional machining tool and fixture, which greatly simplifies the processing steps and shortens the processing time. It is suitable for prototyping parts with complex shapes or that are difficult to be produced via conventional manufacturing. In recent years, 3D printing technology, the best known AM technology, has developed rapidly. Compared with the traditional casting technology, 3D printing technology no longer needs the mold in advance. The shape information can be imported into the machine and then the half-completed product can be automatically processed, which saves the material and time consumed in designing and manufacturing the mold. Considering the complexity of TPMS structure, this research uses the selective laser melting (SLM) technology to produce the F-RD HX.

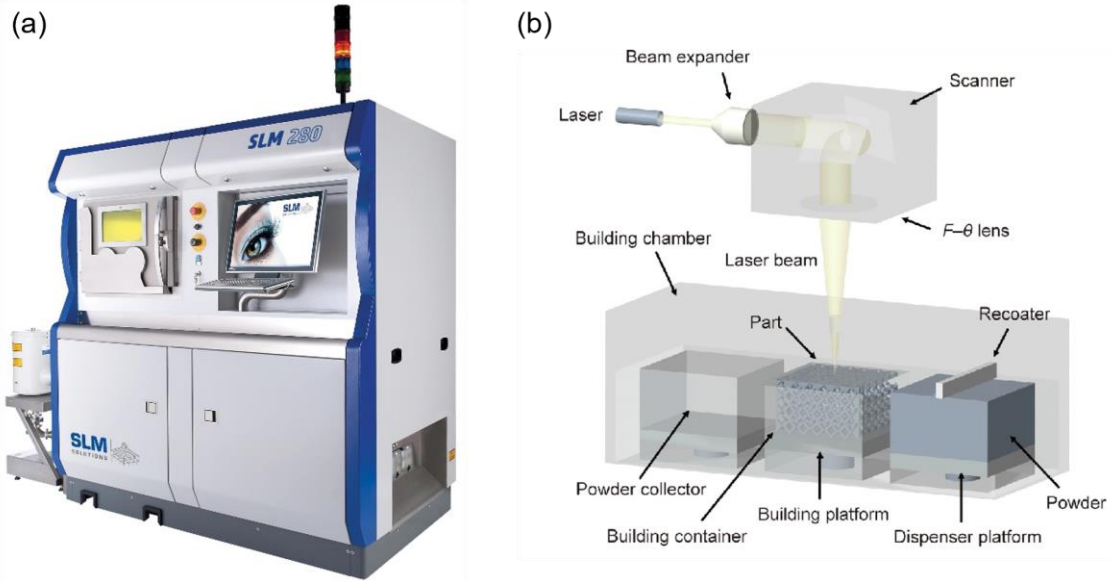


Figure 2.3. (a) SLM printer (source: <https://www.51sole.com/xinxi/128967841.htm>), (b) SLM prints schematics (source: https://www.researchgate.net/figure/Schematic-of-the-SLM-process_fig2_334230008).

SLM is a special 3D-printed AM technology designed to melt and fuse metal powders using high power density lasers (Yap et al. 2015). The high energy laser beam completely melts the metal powder in the protective atmosphere of the laser path, and the molten metal rapidly solidifies. By repeating this step and overlapping layer by layer, a three-dimensional component is finally formed (Zhang et al. 2019), whose schematic diagram is shown above. Because SLM are not limited by the shape of traditional reduction tools, they can be used to process parts that are difficult to manufacture using traditional methods. Murr indicates that AM techniques such as SLM technology show promise in the fabrication of artificial bones and porous scaffolders (Murr 2019).

SLM is now capable of printing and processing copper, aluminum, tungsten and other metal powders (Yap et al. 2015). Among them, aluminum alloy powder is characterized by light weight and good microstructure (Aboulkhair et al. 2019). Zhang used aluminum alloy as material to study SLM printing products. It was proved that SLM processed products have high toughness and corrosion resistance (Zhang et al. 2019; Bobbert et al. 2017; Ponnusamy et al. 2020). In addition, studies have shown that aluminum alloy has excellent thermal conductivity, so it is undoubtedly a good choice to use aluminum alloy to manufacture HXs (Jafari and Wits 2018).

At the same time, SLM has certain limitations. In order to ensure print quality, some key parameters need to be well considered. For example, the laser power, scanning speed, hatch spacing and layer thickness (Yap et al. 2015; Aboulkhair et al. 2019) need to be properly set, otherwise spheroidization, cracking and even printing failure probably occur (Zhang et al. 2019). In addition, for suspended structure, because the bottom surface is supported by loose metal powder,

the powder on the top layer directly melts on the previous powder. The unstable support will cause small displacement of the unsolidified printing body, and the solidified part may be attached by powder. This will increase the surface roughness of the product and reduce the concentricity (Al-Ketan et al. 2020). In terms of manufacturing precision, the diameter of SLM laser molten pool is about 100 microns. The processing accuracy of SLM is considered to be the size of molten pool in calculation, namely $\pm 0.1\text{mm}$.

In order to verify the print quality of the F-RD HX, this research manufactures an F-RD HX and an F-RD array in the same batch. The F-RD HX will be used for heat transfer experiments and the F-RD array will be used for SEM observation.

Chapter 3.

Heat Exchanger Design and Manufacture

This chapter provides a detailed introduction to the design and manufacture of the HX used in the project. After the HX is manufactured through SLM technology, SEM is used to inspect and scan the internal structures of a $3 \times 3 \times 3$ F-RD array for evaluation.

3.1. Heat Exchanger Design

Table 3.1. The design details of F-RD HX.

	Porosity	Unit volume (mm ³)	Unit heat exchange area (mm ²)	Unit surface area-to-volume ratio	Array	Total volume of heat exchanger (mm ³)
F-RD	0.810	336.96	1056.6	1.57	$8 \times 8 \times 5$	233341
S-D	0.810	336.25	1116.6	1.66	$8 \times 8 \times 5$	234217

Table 3.1 presents the design details of the F-RD HX. Similar porosity and array number are maintained between the F-RD and S-D HXs to facilitate a comparison of their respective flow characteristics and heat transfer performance.

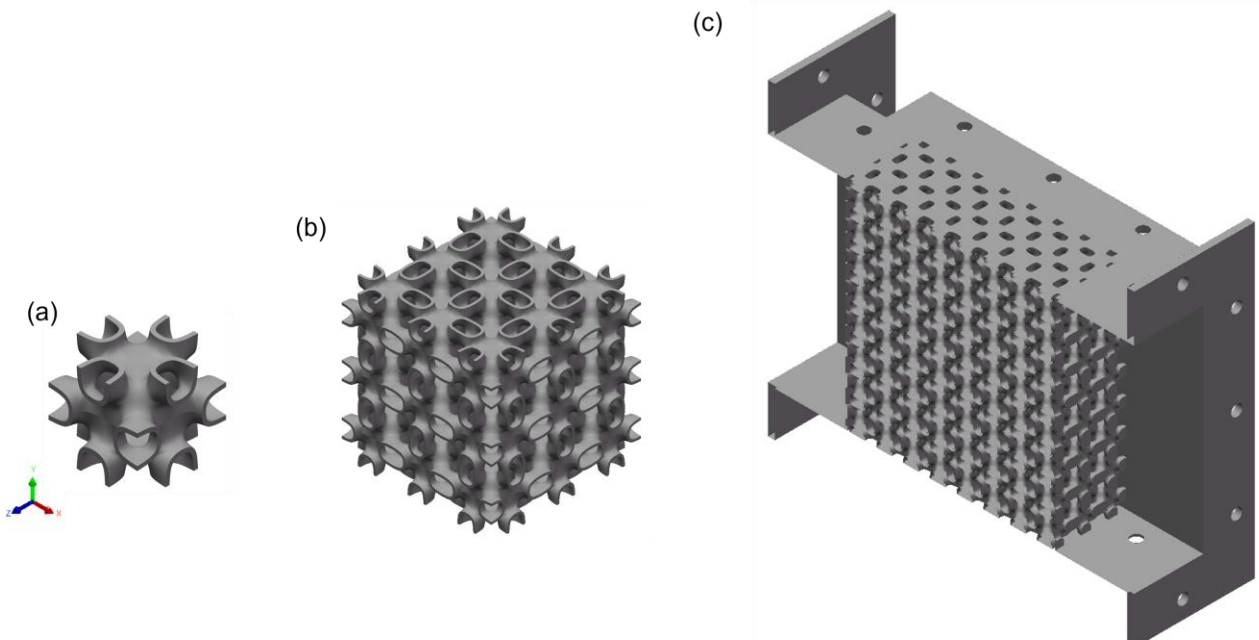


Figure 3.1. F-RD HX models of interest in this study (a) F-RD unit, (b) $3 \times 3 \times 3$ array of F-RD unit, (c) Cross-section of the overall HX.

Using the design of the F-RD HX as an example, Figure 3.1 illustrates the F-RD unit body in (a), a 3x3x3 array of F-RD units in (b), and a CAD cross-section of the overall TPMS HX in (c). To facilitate assembly with the experimental pipeline, a rectangular flange was added to the HX. The inner core arrangement of the HX is 8x8x5, with corresponding dimensions of 96mmx96mmx60mm. The design of the S-D HX also follows a similar approach (Liang et al. 2023).

After completing the CAD design, the TPMS HXs are manufactured using SLM technology. The chosen material is an aluminum alloy powder that offers lightweight and excellent heat transfer performance, with a thermal conductivity of 181 [$W\ m^{-1}\ K^{-1}$]. It is worth noting that SLM printed products may exhibit surface roughness, holes, and cracks, which could compromise the experiment's safety and the data's accuracy. Hence, the SLM printed products will be carried out inspection activities to ensure their quality. During the printing of the entire HX, we also manufacture the 3x3x3 unit array in the same batch. This array is used to evaluate the SLM printing quality through electron microscopy and serves as a representative sample of the HX's internal structure details.

3.2. Manufacturability Evaluation

This section describes the use of SEM to assess fabrication quality. Figure 3.2 (a) shows our measurement object, which is an array of 3x3x3 F-RD units printed in the same batch as the experimental HX in Figure 3.2 (b).

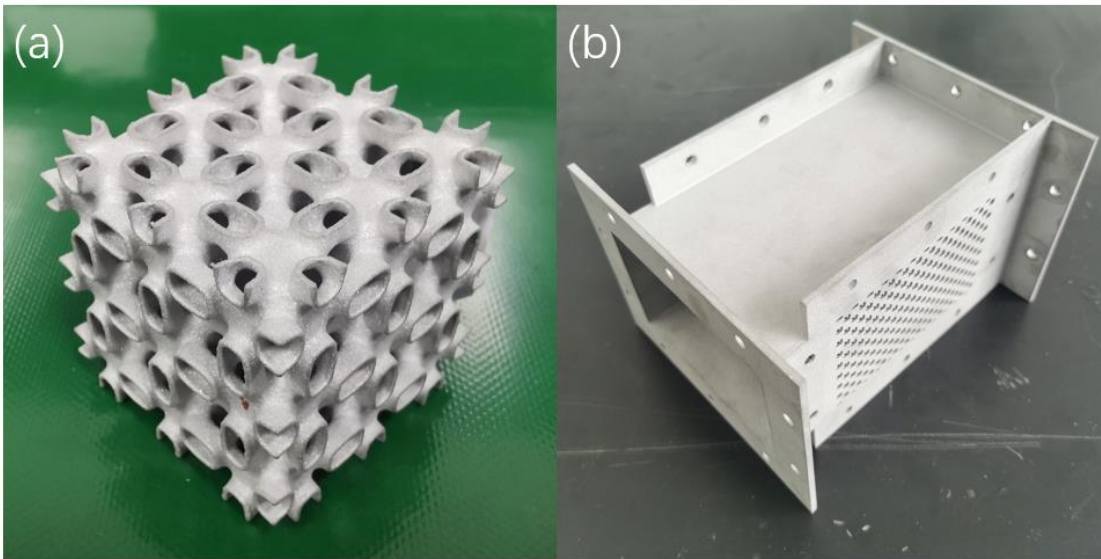


Figure 3.2. Manufactured products, (a) F-RD array, (b)F-RD HX.

The surface characteristics of the F-RD array were analyzed by SEM (Figure 3.3). The dimensional accuracy was evaluated firstly, then the surface morphonology was analyzed. Finally,

the roughness of the bottom and top surface was quantitatively compared. The SEM used is Phenom XL, which can evaluate the surface roughness by measuring Ra and Rz in the selected regions. It also provides software, PhenomImageViewer, for image analysis, which is used to measure dimension.



Figure 3.3. Picture of scanning electron microscope experiment machine.

3.2.1. Dimensional Accuracy

Parameters such as array length, wall thickness and porosity are measured. Some data are presented as mean \pm standard deviation. Table 3.2 shows design and measured parameters of the F-RD Array.

Table 3.2. Parameters of the F-RD array.

Design length (mm)	Measured length (mm)	Design wall thickness (mm)	Measured wall thickness (mm)	Design porosity	Measured porosity
36	35.7 ± 0.1	0.640	0.661 ± 0.032	0.810	0.806

The wall thickness of the structure is obtained by using PhenomImageViewer software to mark the elliptic outer edge of the image. Totally 24 groups of wall thickness data are measured, and the maximum and minimum values are removed. The remaining 22 groups of wall thickness data are used for fitting with the least square method. Then the mean value and standard deviation of wall thickness are obtained. Figure 3.4 shows an example of the wall thickness measurement.

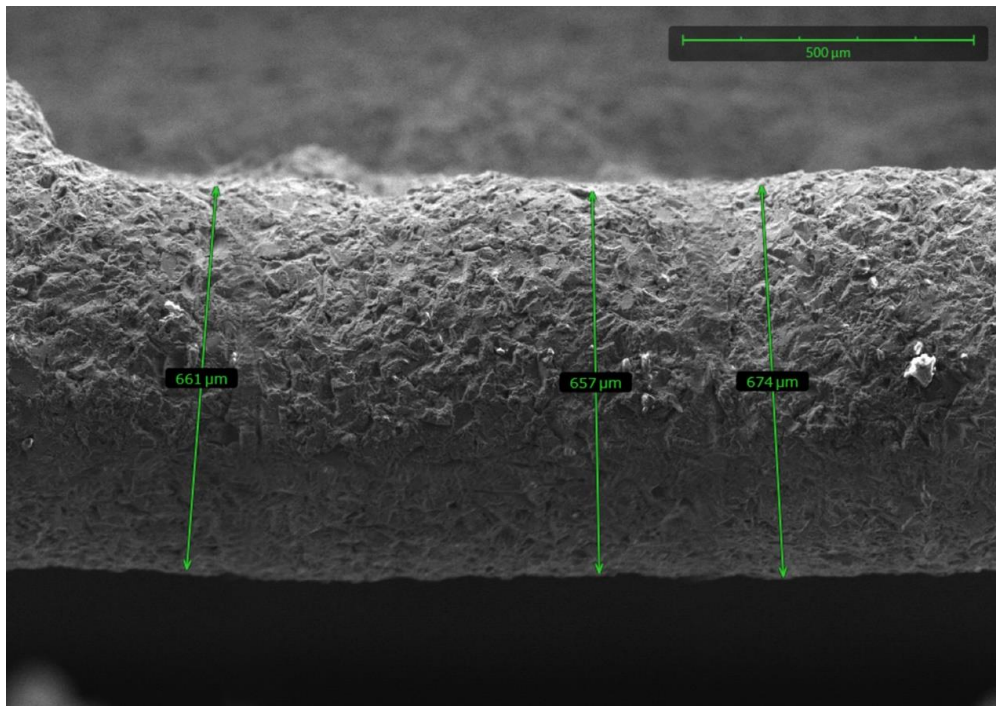


Figure 3.4. Wall thickness selection example.

SEM pictures shows that the array length of F-RD array is about 35.7 mm, slightly smaller than design value. This may be attributed to the phenomenon of thermal expansion and cold contraction in the SLM process. Electronic weighing shows that the mass of the F-RD array is 23.7764 g, and the measured porosity is 0.806, which is smaller than 0.810, indicating that the mass of the F-RD array is larger than the design value. The mean wall thickness of the F-RD array was close to 0.66 mm, 0.02 mm away from the design value 0.64 mm, which shows that SLM processing is relatively accurate.

3.2.2. Surface Morphology

The surface roughness of the printed part is directly related to the printing direction. The surface roughness inside the flow channel will somehow affect the heat transfer performance of the HX. Therefore, it is necessary to evaluate the surface roughness. Figure 3.5 shows how the F-RD array was built. The SEM pictures at the top & bottom (Figure 3.6 (a) and (b)) and the height maps of the top and bottom central low region are as follows (Figure 3.6 (c) and (d)):

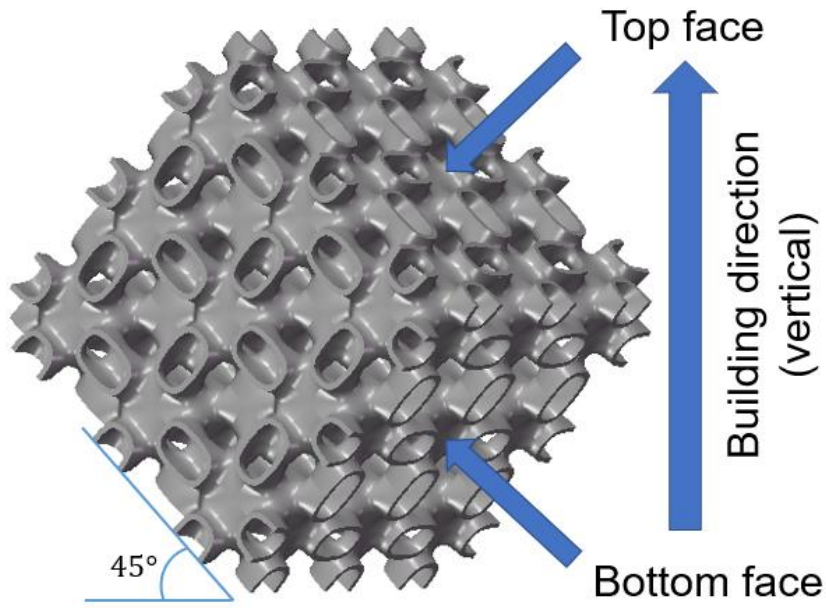


Figure 3.5. Building direction of F-RD array.

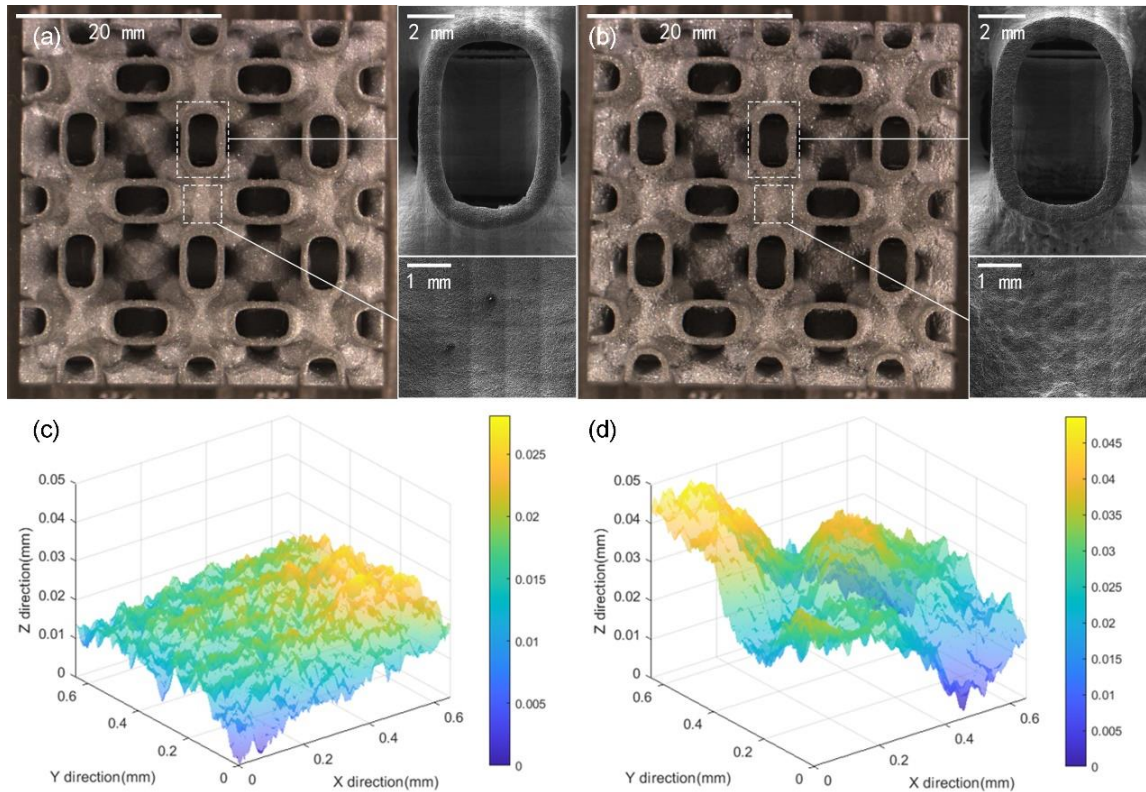


Figure 3.6. SEM pictures at (a) Top of F-RD array, (b) Bottom of F-RD array, (c) height map of top surface (500x), (d) height map of bottom surface (500x).

Ra and Rz values are used to describe the surface roughness (Figure 3.7 (a) and (b)): The sampling length is denoted as l , and the surface contour of l is obtained.

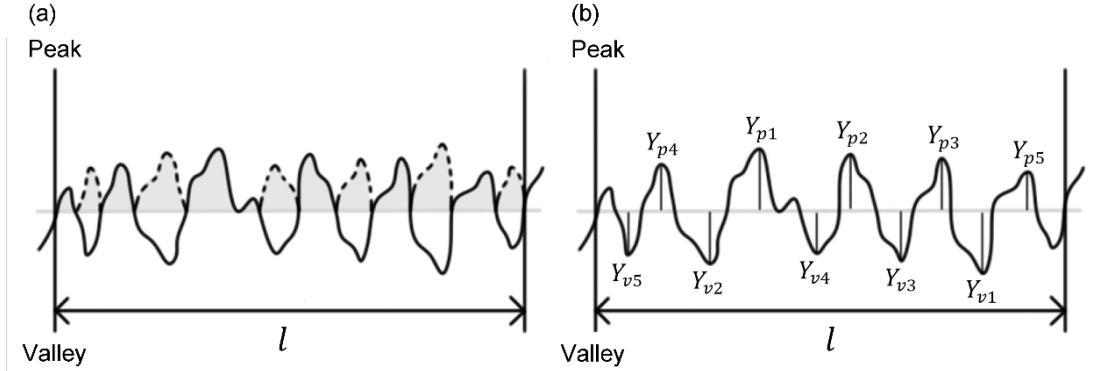


Figure 3.7. (a) Definition of Ra, (b) Definition of Rz.

$$Ra = \frac{\int |f(x)| dx}{l} \quad (1)$$

$$Rz = \frac{|Y_{p1} + Y_{p2} + Y_{p3} + Y_{p4} + Y_{p5}| + |Y_{v1} + Y_{v2} + Y_{v3} + Y_{v4} + Y_{v5}|}{5} \quad (2)$$

The SEM was used to photograph the low region in the center of four elliptical holes of the same F-RD array to measure the surface roughness. The average Ra of the top surface was $17.8216 \mu m$ and the average Rz was $6.07 \mu m$. The average Ra of the bottom surface was $28.28 \mu m$ and the average Rz was $9.1 \mu m$. Obviously, the top surface is smoother than the bottom because the top is supported by solidified metal, while the bottom is supported by loose powder. According to the periodicity of F-RD structure, rough surfaces will appear at the similar location in each unit.

3.2.3. Defect Observation

For the F-RD array, there are no serious defects such as cracks and through-holes on the surface. The existence of thickened wall thickness and rough surfaces does not affect the integrity of the structure. Based on the above results, the printing of the F-RD array is qualified. For the F-RD HX, similar to F-RD array, no problem on the surface as well. Then ventilation test is carried out. When ventilating the cold flow channel, no gas flow in the hot flow channel was escaped. It is found that there is no leakage phenomenon, which proves the good integrity of the F-RD HX.

Based on the analysis and detection of F-RD array, it can be concluded that the internal problems of F-RD HX are the same as those of F-RD array. It is expected that the rough surface

will somehow affect the experimental results, so that the experiment results will be biased within a certain range. Overall, the printing error is within the range of SLM machining accuracy and deviations between the printed part and the design model are insignificant. The printing quality of the F-RD HX is acceptable.

Chapter 4.

Numerical Simulation of Heat Transfer Process

In this chapter, Ansys-CFX, a computational fluid dynamics software, will be used to perform numerical simulation on the F-RD and S-D HXs. This will allow us to understand and compare their heat transfer characteristics and analyze the fluid flow mechanism as a means of interpreting experimental results. The chapter will cover the introduction of the simulation model, guidance on mesh rendering, details of CFX pre-processing, discussion of numerical analysis results, and an explanation of the fluid flow mechanism within the HXs.

4.1. Numerical Simulation Model Design

To reduce the cost of numerical calculations, the actual HX model is simplified to a 3x3x1 array with adiabatic transitional channels, as the work of Liang (Liang et al. 2023). The translational periodicity conditions are provided at the top and bottom of the calculation domain. As the S-D HX has been reported to possess excellent heat transfer performance in TPMS HXs (Liang et al. 2023), an S-D HX of the same size is designed to compare with the heat transfer performance of F-RD. Table 4.1 provides the design details.

Table 4.1. *Simulation model design details.*

Porosity	Unit volume (mm ³)	Unit heat exchange area (mm ²)	Unit surface area-to- volume ratio	Array
F-RD	0.81	336.96	1056.6	1.57
S-D	0.81	336.25	1116.6	1.66

Figure 4.1 depicts the simplified (a) F-RD and (b) S-D HX models designed in SolidWorks. The red arrow indicates the hot fluid inlet, while the blue arrow represents the cold fluid flow direction. The four outer blank frames represent the adiabatic transitional channel, which stabilizes the fluid before flowing into the HX. The solid wall is divided into two surfaces in different colors: the red surface represents the region in contact with the hot flow, and the blue represents the area in contact with the cold flow.

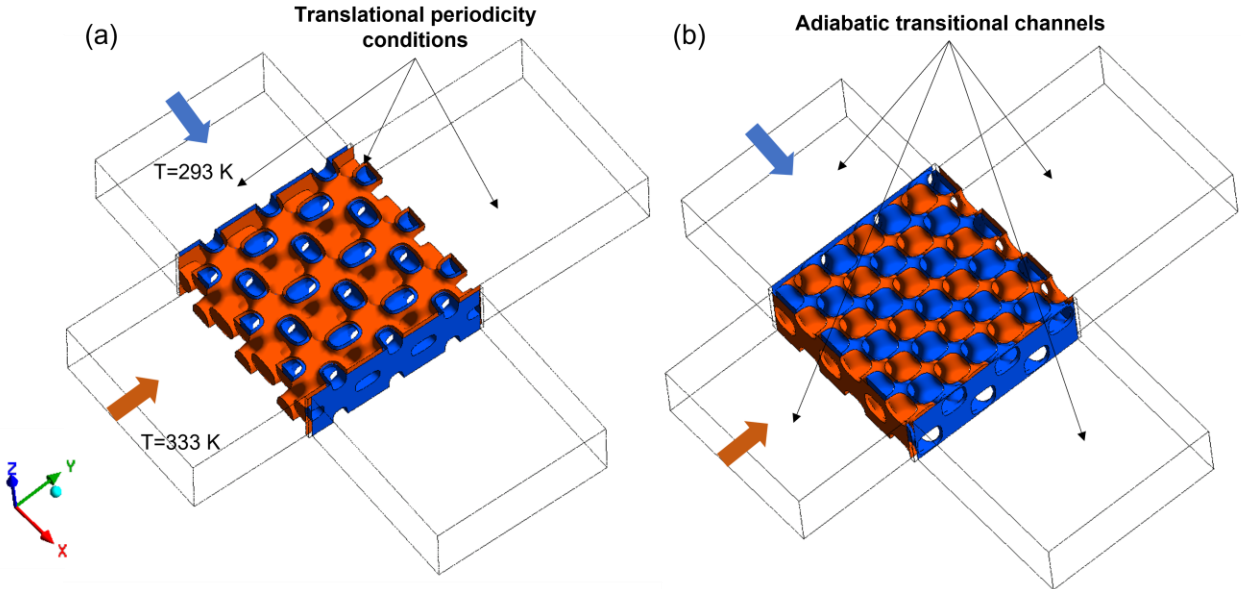


Figure 4.1. The $3 \times 3 \times 1$ TPMS unit array models of numerical simulation (a) F-RD HX, (b) S-D HX.

4.2. Meshing of Computational Domain

As the introduction of CFD technology in Section 2.2, drawing grids for the calculation domain of the simulation model is an important part of the technology. The Ansys-ICEM will be used to mesh the model and finally output the .cfx5 mesh file.

ICEM is a computer-aided engineering software primarily used for 3D mesh generation and geometric model preprocessing for numerical simulation models. The main steps of the mesh division process are illustrated in Figure 4.2.

Numerical Simulation Model Meshing Steps

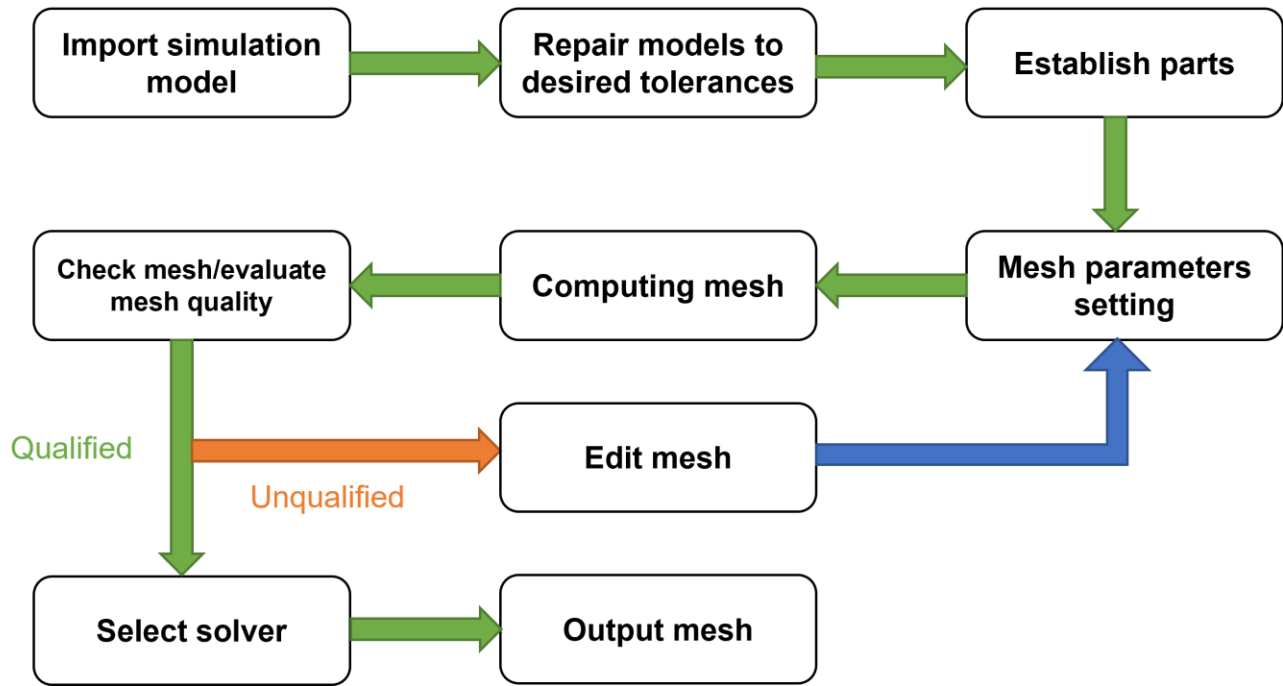


Figure 4.2. Numerical simulation model meshing steps.

First, the simulation model designed in advance is imported into ICEM, and an appropriate tolerance is selected for model repair. Parts of the repaired model are then built, and each part becomes a computational domain. When dividing parts for a HX, it is necessary to differentiate between the hot and cold flow domains and the solid domains and create solid sections in specific areas. Certain geometries, such as lines and points, can be hidden during part division so that all parts only contain surface geometry. Next, mesh parameters are set and the parameter size is adjusted to calculate the mesh according to the calculation needs. After the mesh calculation is completed, the mesh information and quality are checked and evaluated. Incorrect mesh is repaired and edited according to project requirements. Generally speaking, smaller parameters generate more elements, resulting in a more accurate calculation, but also increasing the required calculation time. Therefore, scholars balance calculation accuracy and cost and choose the appropriate number of mesh to achieve the desired calculation accuracy and improve calculation efficiency. Among the common methods, selecting the number of mesh based on the convergence curve is popular. The simulation results are monitored under different element numbers, and the convergence curve is drawn with a certain index as an example. Once a satisfactory mesh is obtained, a solver is selected and the mesh is outputted.

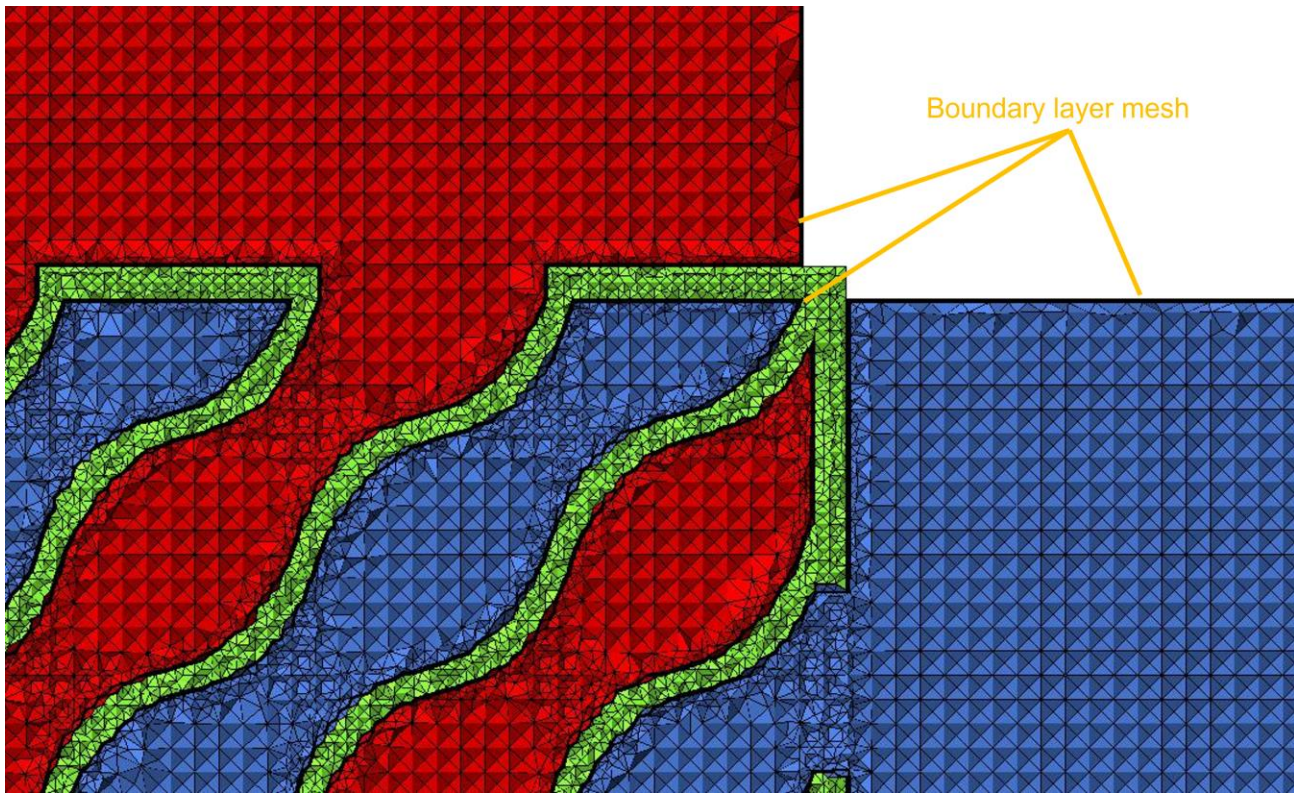


Figure 4.3. Mesh detail of a section inside the S-D HX.

This research aims to mesh the simplified HX model designed in Section 4.1 by following the above steps. After creating all the parts, boundary layer mesh will be used to capture flow information of the boundary layer. Other computational domains will use relatively larger mesh to reduce the number of element and improve computational efficiency. The design parameters for the boundary layer mesh are a height of 0.005 mm, a height ratio of 1.1, and 10 layers. Figure 4.3 illustrates the S-D simulation model using ICEM's "manage cut plane" function to show the mesh inside the HX. The red part represents the hot flow domain, the blue part represents the cold flow domain, the green part represents the solid domain, and the thicker black line segment represents the fine boundary layer mesh.

4.3. Ansys-CFX Pre-processing

As mentioned in Section 2.2, CFX-preprocessing mainly includes defining the calculation domains of the HX, defining the interface between solid and flows, setting simulation parameters, and setting initial conditions and solvers.

Table 4.2. Grid independence check results for the F-RD HX.

The number of elements	The average temperature in cold solid (K)	The average temperature in hot solid (K)
3194939	311.9	312.0
3232599	312.0	312.0
9846918	311.9	312.2
13901935	312.2	312.2
13988173	312.2	312.2
27072434	312.2	312.2

In this study, the calculation and junction domains are defined according to project requirements. As shown in Figure 4.1, the inlet temperature of the HX is set to 333 [K] for the hot flow and 293 [K] for the cold flow, while the outlet pressure is atmospheric. The solid domain is composed of heat-conducting aluminum metal with a conductivity of 181 [$Wm^{-2}K^{-1}$]. The working fluid is defined as an ideal gas, with transport properties and thermal conductivity defined using the Sutherland formula. Translational periodicity conditions are set on the boundaries of the hot and cold flow channels, as well as the solid domain boundaries, to simulate infinitely repeating geometric structures. This approach reduces the computational domain to enhance the simulation efficiency when simulating larger systems. After analyzing the grid independence check results for the F-RD HX in Table 4.2 and taking into account the calculation efficiency and accuracy, it was determined that the F-RD HX uses 13.9 million mesh elements, while the S-D HX uses 13.3 million mesh elements (Liang et al. 2023). Finally, appropriate solver parameters are selected according to laboratory conditions.

4.4. Numerical Simulation Verification

In order to verify our simulation models, two heat transfer indicators, namely overall heat transfer coefficient U and heat transfer effectiveness ε , are selected in this section to compare the experimental results (see Chapter 5 for details of experiment) with the numerical simulation results.

The overall heat transfer coefficient (U), is a measure of the overall rate of heat transfer across a surface or a boundary between two fluids. Typically, heat exchangers with larger U values are more favored. The heat transfer effectiveness (ε) is a measure of how effectively heat is transferred from one fluid to another or from a solid surface to a fluid. It is a dimensionless quantity that compares the actual heat transfer rate to the maximum possible heat transfer rate between the two fluids or between the solid surface and the fluid. Their definitions will be introduced in detail in Section 5.2.

The overall heat transfer coefficient (U) is defined as follows,

$$U = \frac{Q_{avg}}{LMTD * A * \Phi} \quad (3)$$

Where Φ is the correction coefficient (see Section 5.2 for the details), A is the average heat transfer area of hot and cold channels, which are measured by CAD software. Logarithmic mean temperature difference LMTD is defined by following equation,

$$LMTD = \frac{(T_{hot,in} - T_{cold,out}) - (T_{hot,out} - T_{cold,in})}{\ln(\frac{T_{hot,in} - T_{cold,out}}{T_{hot,out} - T_{cold,in}})} \quad (4)$$

Taking some of them as examples, $T_{hot,in}$ represents the fluid temperature at the inlet of the hot channels, $T_{cold,out}$ represents the fluid temperature at the outlet of the cold channels. The average heat transfer rate Q_{avg} of hot and cold channels is defined as follows,

$$Q_{avg} = \frac{Q_{hot} + Q_{cold}}{2} = C_p * \dot{m} * |T_{in} - T_{out}| \quad (5)$$

\dot{m} is the mass flow, which is determined by the experimental conditions. C_p is determined by the physical properties of the fluid. The heat transfer effectiveness (ε) is defined as following equation,

$$\varepsilon = \frac{Q_{avg}}{Q_{max}} = \frac{Q_{avg}}{(C_p * \dot{m})_{min} * (T_{hot,in} - T_{cold,in})} \quad (6)$$

Since the numerical simulation is not a full model simulation, the focus of attention is on the change trend of the experimental results and numerical simulation results. The numerical simulation is considered reasonable if the simulation results show a similar variation trend to the experimental results.

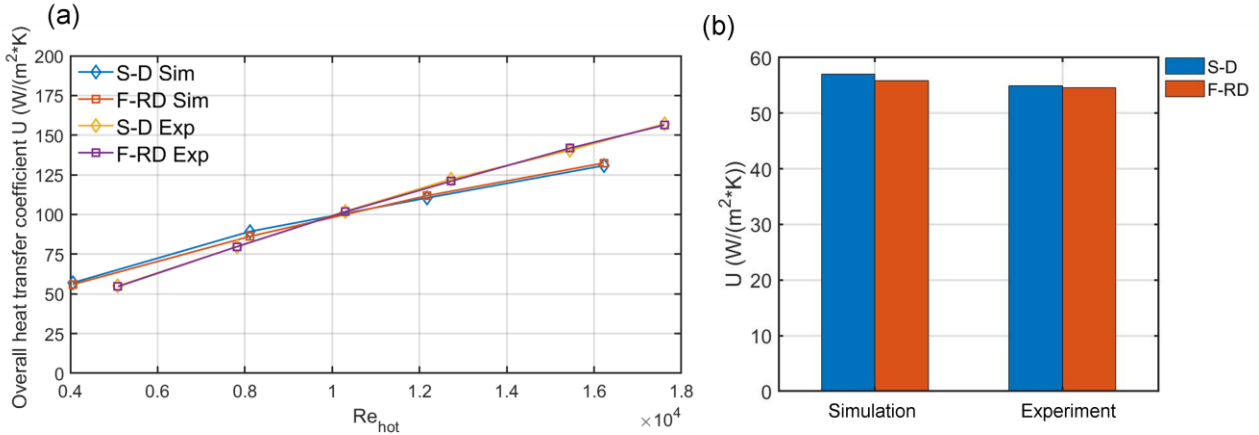


Figure 4.4. Comparison of overall heat transfer coefficient U between simulation and experiment, (a) U vs Re , (b) U under the hot flow with a velocity of 1 m/s.

The numerical simulation is carried out under the working condition of the inlet flow rate of 1-6 [m s^{-1}], and the experimental flow rate is carried out under the working condition of 20-70 [$\text{m}^3 \text{h}^{-1}$]. The Reynolds number is defined by

$$Re = \frac{\nu D_h}{\nu} \quad (7)$$

where ν , D_h , ν are flow velocity, channel hydraulic diameter and kinematic viscosity respectively (see Section 5.2 for the details).

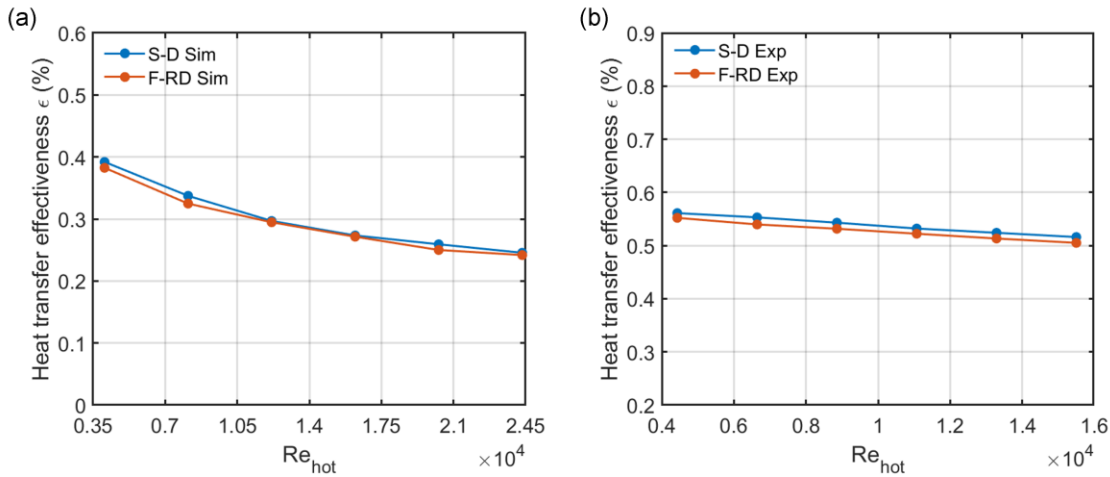


Figure 4.5. Comparison of heat transfer effectiveness ϵ between simulation and experiment, (a) numerical simulation results, (b) experimental results.

Figure 4.4 compares the overall heat transfer coefficient U of numerical simulation and experiment, and Figure 4.5 shows the comparison of heat transfer effectiveness ϵ . The U increases with the increase of Reynolds number, and the ϵ decreases with the increase of Reynolds number.

Figure 4.4 (a) illustrates the variation of the U value under different operating conditions, while (b) focuses on the U value at a flow velocity of 1 m/s. The simulation results align closely with the experimental data in terms of trends and calculated U values. The simplified model proves to be a reliable predictor of the U value, primarily because the overall heat transfer coefficient U removes the impact of heat transfer area on performance. Figure 4.5 (a) and (b) reveal similar trends between simulation and experimental results, with the notable disparity in values attributed to the shorter flow path in the simplified simulation model. In conclusion, the consistency observed between numerical simulation and experimental results validates the effectiveness of the simulation approach.

4.5. Analysis of Numerical Simulation Results

The simulation results were obtained in CFX-Post software. Typically, the HX with higher heat transfer effectiveness and lower pressure drop penalty is preferred. Taking the simulation condition where the flow velocity in the hot and cold domain is 1 [$m s^{-1}$] as an example, the overall heat transfer coefficient U of F-RD and S-D are 56 [$W m^{-2}K^{-1}$] and 57 [$W m^{-2}K^{-1}$]. This theoretically shows that the S-D HX and F-RD HX have similar heat transfer performance. The HX will be dissected and analyzed in more detail in order to clarify its flow mechanism.

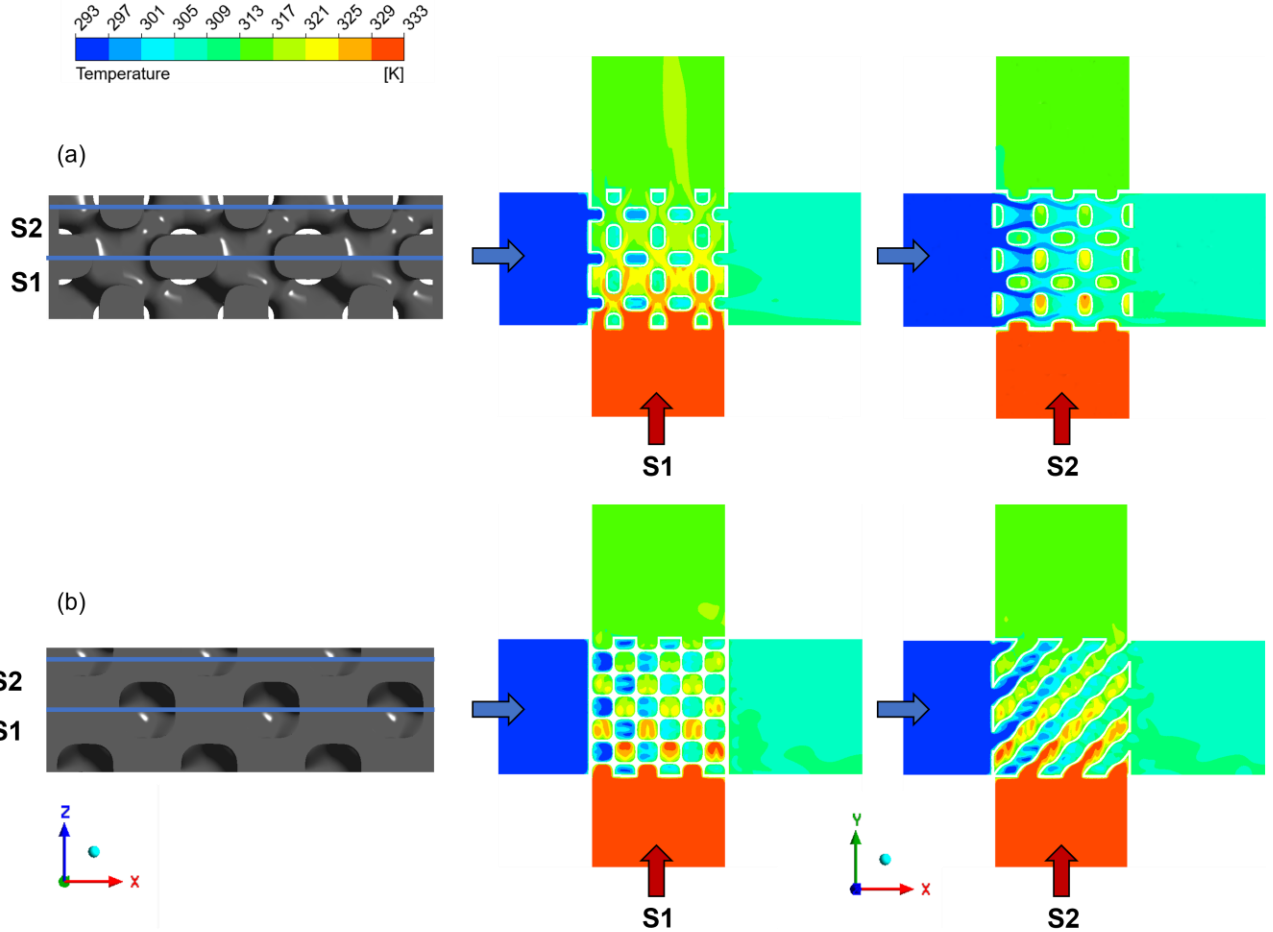


Figure 4.6. Fluid temperature distribution in the internal section of the HX, (a) F-RD HX, (b) S-D HX.

Figure 4.6 illustrates the diagram of fluid temperature within the F-RD and S-D HXs, where the white part represents the solid wall. It can be observed that the internal fluid flow in the F-RD and S-D HXs is highly complex, with the fluid constantly being interrupted by the wall, leading to changes in flow direction and reflecting the three-dimensional flow pattern of the TPMS HX. In section 1 of the F-RD HX, a relatively straight-through flow channel is found in the cold domain, while in section 2, the hot domain is a straight-through flow channel. The direction of fluid flow constantly changes between straight-through and non-straight-through inside the F-RD HX. Although the straight-through flow channel is not conducive to heat transfer (Liang et al. 2023), the blocking area along the flow direction is large, which significantly promotes flow impingement, thereby enhancing heat transfer. However, the wall is always perpendicular to the main flow direction, which hinders the flow of fluids, and it will inevitably lead to a large pressure drop. There is no straight-through flow channel inside the S-D HX. In section 1, the hot and cold flows are constantly interrupted by the wall, forcing the fluid to change flow direction. In section 2, the hot and cold fluids flow at a 45-degree angle, and when reaching the hot and cold outlets, the walls force the fluids to flow up or down. The cold and

hot fluids of F-RD and S-D have similar temperature results, indicating that the two types of HXs have similar heat transfer performance.

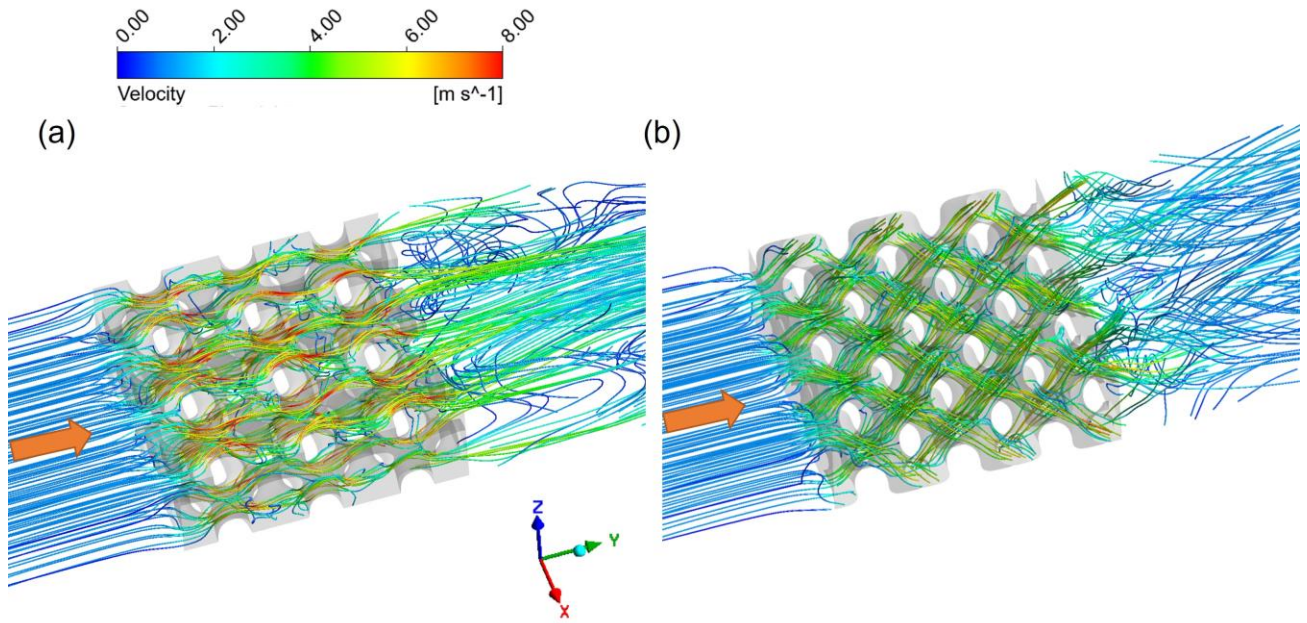


Figure 4.7. Velocity streamline of the heat flow inside the HX, (a) F-RD HX, (b) S-D HX.

Figure 4.7 shows the velocity streamline of the hot flow inside the HX. Similar to other TPMS HXs, both the (a) F-RD and (b) S-D HXs exhibit three-dimensional flow patterns, albeit with different degrees of complexity, which are reflected in the Figure 4.7 as the cold and hot flows are separated by walls, and the flow channels are intertwined, heat exchange is performed in a three-dimensional space, the main flow is constantly changed to form a large-scale turbulent flow, and the continuous interaction between the fluid and the solid wall enhance heat exchange between the cold and hot flows. Meanwhile, it is found that the F-RD HX has more red highlighted streamlines than the S-D HX, so indicating that the fluid in the F-RD HX has a greater average velocity. According to the Bernoulli equation (Qin and Duan 2017), the greater the flow velocity, the lower its pressure, so it can also be judged that F-RD HX induces a larger pressure drop.

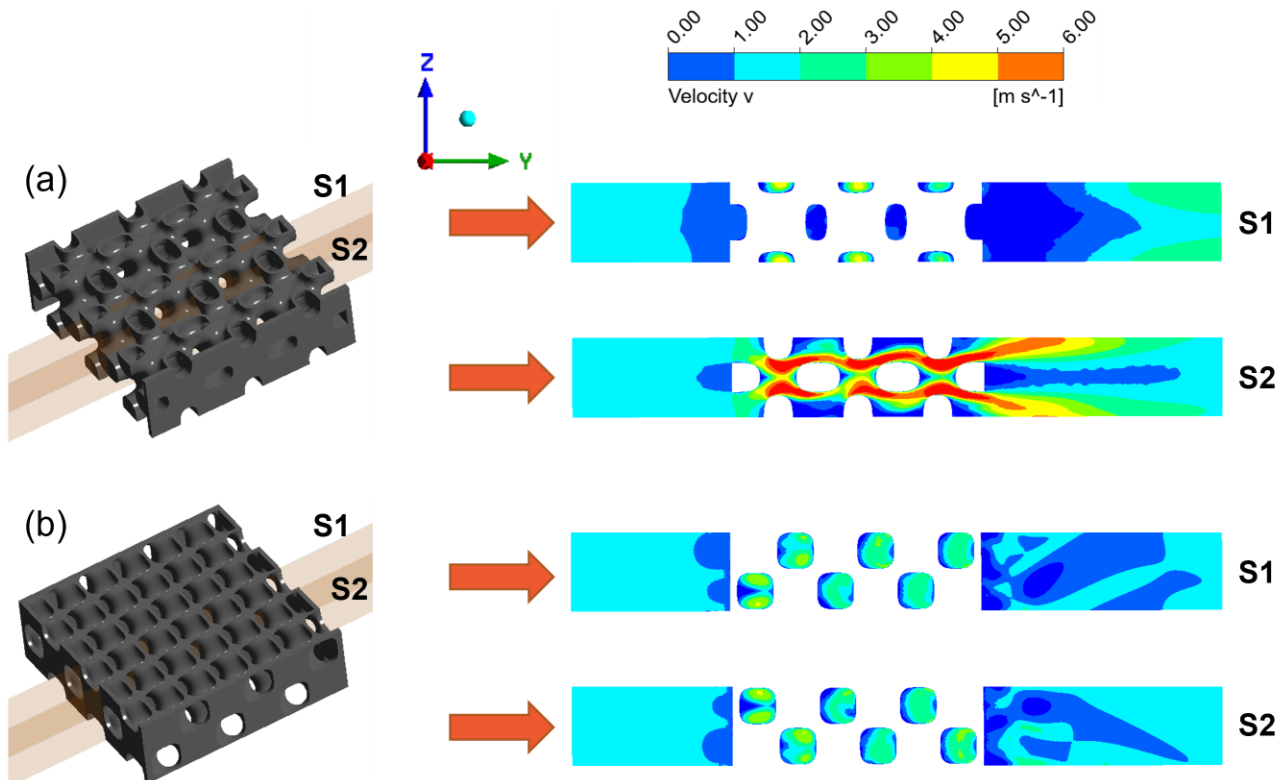


Figure 4.8. The velocity distribution of the internal section of the HX along the y-axis, (a) F-RD HX, (b) S-D HX.

Figure 4.8 shows the cross-sectional velocity distribution of the hot flow inside the F-RD and S-D HXs along the y-axis direction. Consistent with the analysis in Figure 4.6, it is shown in Figure 4.8 (a) that the hot flow of the F-RD HX indeed has a straight-through channel in the S2 cross section. The flow is ejected out of the channel with obvious acceleration. However, there are still a large portion of fluids blocked by the wall, which reduces the fluid energy at the interaction point, resulting in larger pressure drop. The velocity distribution under different sections of F-RD has greatly differences. In contrast, the fluid velocity distribution of different sections in S-D HX has a similar level of variation. This shows that there is a great difference in the fluid flow mechanism between the F-RD HX and the S-D HX. Combining with Figure 4.7 and Figure 4.8, it can be found that the three-dimensional flow pattern in S-D HX is more distinct, and the fluid is distributed more uniformly among the individual pores.

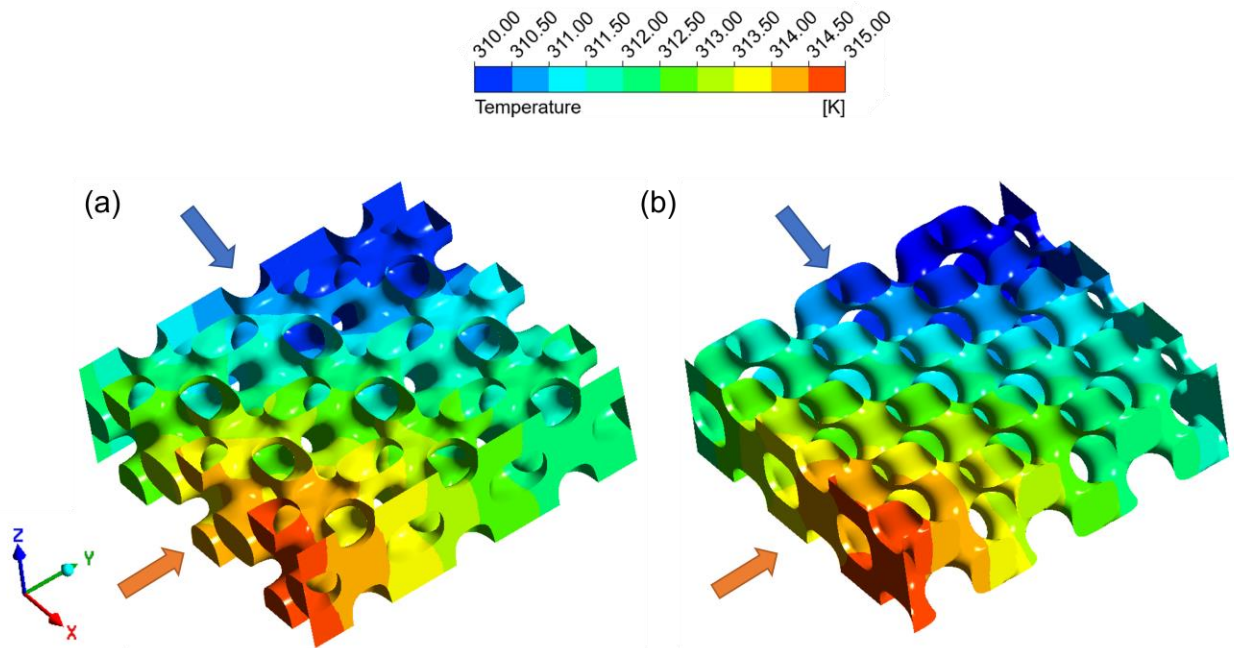


Figure 4.9. Temperature profile of the solid region of the HXs, (a) F-RD HX, (b) S-D HX.

The temperature distribution diagram of the solid domain of the HX is depicted in Figure 4.9, with blue arrows indicating the cold flow inlet and red arrows indicating the hot flow inlet. The upper right corner is marked with a dark blue area, representing the lowest temperature because it is where the cold air flows in and the outlet of the hot air. The coldest hot and cold fluids meet in this area, resulting in the lowest temperature. In comparison, the lower left corner has the highest temperature because it is where the hot air flows in and the cold air flows out. It can be observed that there is an increasing trend in temperature from the upper right to the lower left. Regardless of whether it is the F-RD or the S-D HX, their solid domains exhibit similar temperature distributions. Additionally, the temperature data on the surface of the F-RD and S-D HXs in the experiment are compared in Section 5.1, and find that the relative temperature of the five thermocouple points in the experiment is consistent with the simulation results.

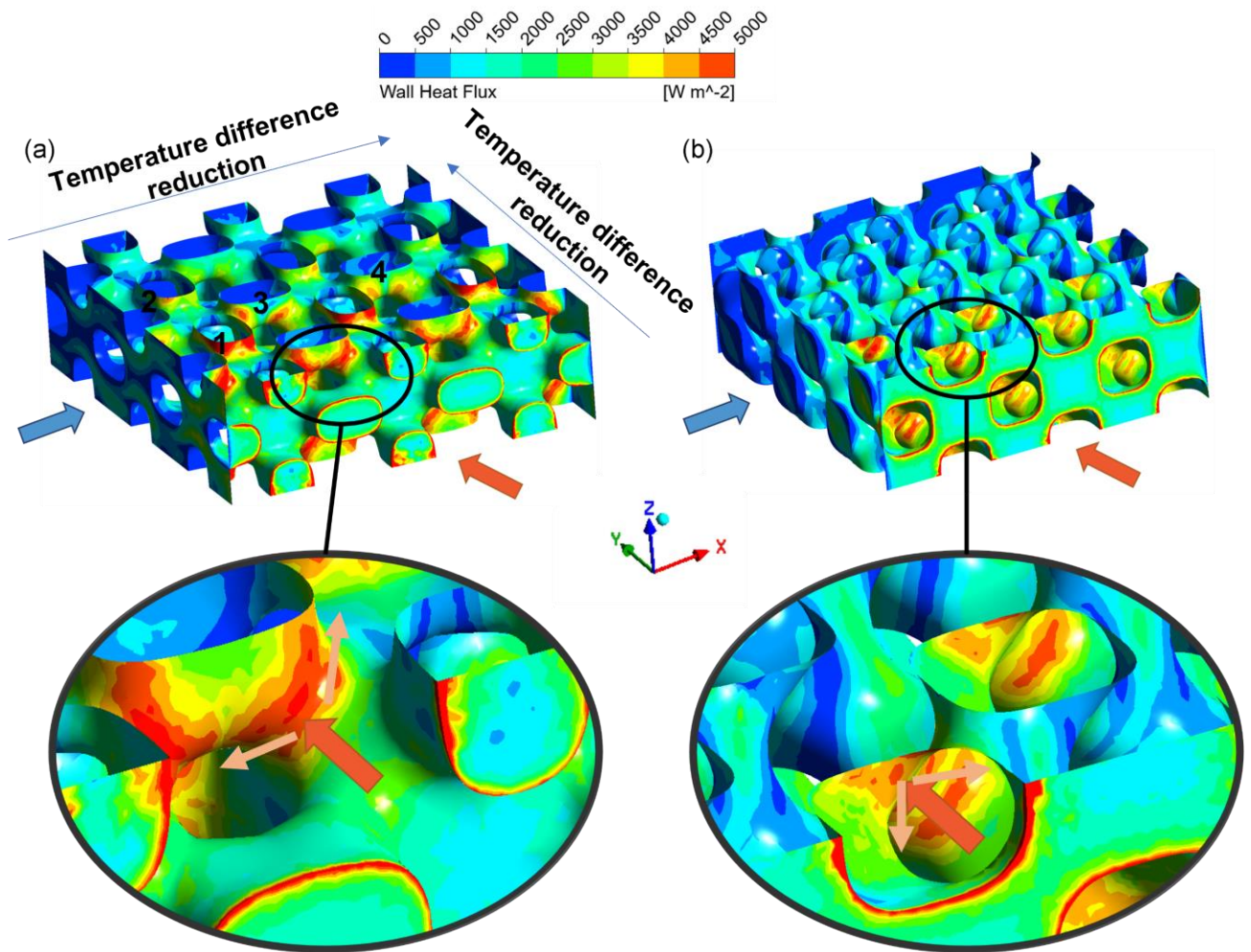


Figure 4.10. Heat flux on the solid surface of HX cores, (a) F-RD HX, (b) S-D HX.

Figure 4.10 (a) and (b) illustrate the heat flux distribution details on the solid surface of the F-RD and S-D HX. The high heat transfer regions for both types of HXs are concentrated where the heat flow initially enters the interior of the HX and interacts with the solid surfaces, particularly in the curved areas of the flow channel or areas that block fluid movement where the interaction of solid and fluid causes the fluid to hit the wall, bifurcate, and change the direction of flow, leading to strong turbulence and efficient heat transfer. Conversely, the opposite side of the high heat transfer region is low-level heat transfer region, as the fluid interacts less with the solid domain. Interestingly, the high heat transfer region of the F-RD HX is more evident than that of the S-D HX. This may be due to the fact that the internal structure of the S-D HX causes the fluid to flow diagonally after entering the HX (as shown in Figure 4.3, Figure 4.7 and Figure 4.6), resulting in a relatively small velocity component directly facing the solid, and inducing a relatively weak interaction between solid and air. However, in the F-RD HX, the fluid impinges more directly with the solid domains, resulting in more intense interaction and stronger wall heat flux.

It is worth noting that in the solid part away from the hot flow inlet, there are almost no high heat transfer areas because the temperature difference between the cold and hot flows in this region is small, significantly reducing the heat exchange. The heat transfer on the solid surface becomes stronger as the temperature difference between the hot and cold flows increases. Taking the F-RD HX as an example, the inlet of the hot and cold flows is located in the lower left corner, where the cold flow with the lowest temperature intersects with the hot flow with the highest temperature, resulting in the highest temperature difference. Along the y-axis direction, the temperature difference between the hot and cold air continuously decreases, leading to a higher heat flux at point 1 compared to point 2. Similarly, the intersection of the cold flow with the highest temperature and the hot flow with the lowest temperature is located in the upper right corner, resulting in the lowest temperature difference. Along the x-axis direction, the temperature difference continuously decreases, resulting in a decrease in heat flux, and the heat flux at point 3 is lower than that at point 4.

In terms of pressure drop penalty, the simulation results indicate that at the cold flow channel, ΔP_{S-D} is 55.9 [Pa], ΔP_{F-RD} is 94.1 [Pa], while at the hot flow channel, ΔP_{S-D} is 50.0 [Pa], ΔP_{F-RD} is 77.2 [Pa]. Therefore, in terms of pressure drop, S-D HX is better than F-RD HX, regardless of whether it is at the cold flow channel or the hot flow channel. The simulation results about pressure drops are consistent with the above analysis.

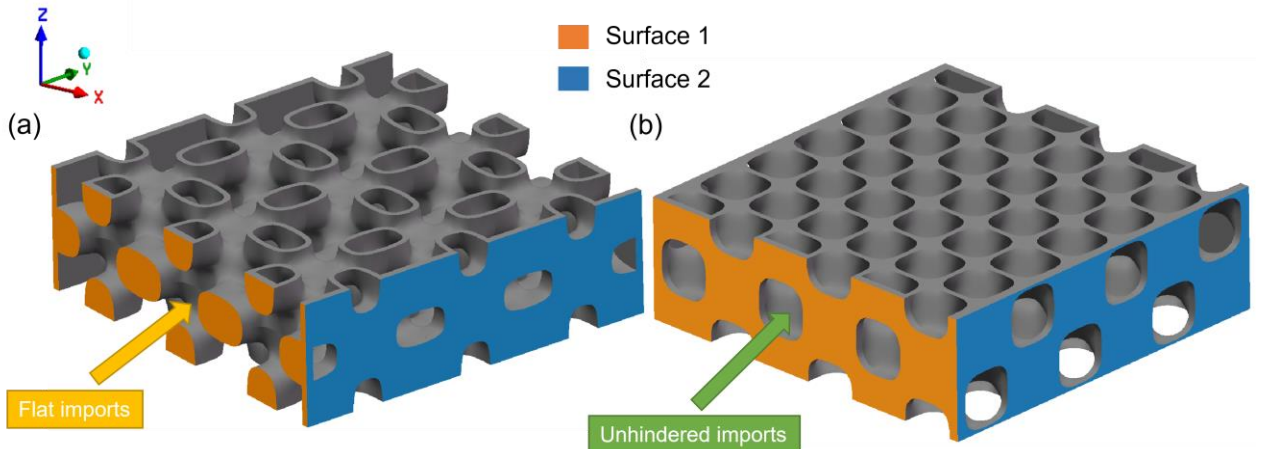


Figure 4.11. The core detail of the numerical simulation models, (a) F-RD HX, (b) S-D HX.

An important factor affecting the pressure drop is the blockage caused by the inlet baffle, which leads to a significant loss of energy in the fluid and a corresponding reduction in fluid pressure. Figure 4.11 shows the core section of the simulation model. The areas of Surface 1 and Surface 2

are equal to the blockage area of the hot flow inlet and cold flow inlet, respectively. Using SolidWorks to measure the blockage at the inlets of the simulation model, the following data were obtained:

$$Area_{F-RD-S1} = 172 \text{ mm}^2, Area_{F-RD-S2} = 363 \text{ mm}^2$$

$$Area_{S-D-S1} = 291 \text{ mm}^2, Area_{S-D-S2} = 289 \text{ mm}^2$$

Taking $Area_{F-RD-S1}$ as an example, it was marked as Surface 1 in the F-RD simulation model.

Through Figure 4.11 and the area data, it can be concluded that at the cold flow channel, the blockage surface area (363 mm^2) of the F-RD simulation model's core is much larger than that of the S-D simulation model's blockage surface area (289 mm^2). Undoubtedly, under the same inlet flow rate, the larger the blockage area, the greater the resistance to the fluid, resulting in a more significant pressure drop. However, the blockage area F-RD (172 mm^2) of the hot end is smaller than that of S-D (291 mm^2). Observing the geometric structures of the two, it is not difficult to find that although the blockage area at the hot flow channel of F-RD is smaller, the structure is similar to the new blockage area because the imports is relatively flat. This similarity causes the hot flow to experience a similar blockage as it flows into the HX, thereby increasing the pressure drop to a certain extent. Conversely, under the same viewing angle, S-D HX has relatively unhindered imports.

It is worth noting that the internal geometry of both the S-D and F-RD HXs' cores is symmetrical. Therefore, theoretically, if the baffle area is similar, there should be similar pressure drops in both the hot and cold channels. This has been verified in the numerical simulation results of the S-D HX, where the pressure drops of both the cold and hot channels are similar. However, due to the different baffle areas, the pressure drops of the F-RD HX's hot and cold flow channels are significantly different.

4.6. Summary of Numerical Simulation

Therefore, based on the analysis above, it can be concluded that the S-D and F-RD HXs have similar overall heat transfer performance, but differ significantly in their internal flow mechanisms. Unlike the S-D HX, the working fluid in the F-RD HX does not exhibit significant three-dimensional flow pattern. The F-RD HX relies on the continuous impingement of the fluid and solid wall to enhance heat exchange, while the S-D HX relies on the large-scale three-dimensional flow inside, where the fluid is continuously bifurcated to enhance heat exchange performance. Additionally, the working fluid of S-D HX flows along the diagonal, which increases the heat transfer path, resulting in more heat

transfer time. In terms of pressure drop, the S-D HX has similar blockage areas for the hot and cold channels, and its internal units are symmetrically, and they are arranged regularly, resulting in similar pressure drops for both hot and cold flows. However, in the F-RD HX, although its unit is symmetrical, there is a significant difference in the blockage areas of the hot and cold channels, leading to different pressure drops for each flow. Additionally, due to the impingement effect, the pressure drops of the F-RD HX are larger than that of the S-D HX.

Chapter 5.

Heat Transfer Experiment

In this chapter, steady-state heat transfer experiments on the F-RD HX are conducted. Specifically, it includes the introduction to the experimental setup, the uncertainty analysis, the data processing and analysis of the experimental results.

5.1. Heat Transfer Experimental Design

As shown in Figure 5.1 (a), the experimental device is composed of hot and cold flow channel. The fluid in the channel is supplied by the air compressor shown in Figure 5.1 (b) and flows into each pipeline after passing through the air dryer shown in Figure 5.1 (c). Each channel is composed of a pressure reducing valve, a flow control valve and a thermal flowmeter, with an accuracy of 2%. During experiments, the hot air at the inlet of HX is maintained at about 75 °C, here can be achieved by adjusting the voltage of the heater on hot flow pipeline. Additionally, the pressure at 0.15 [Mpa] is maintained by adjusting the reducing valve.

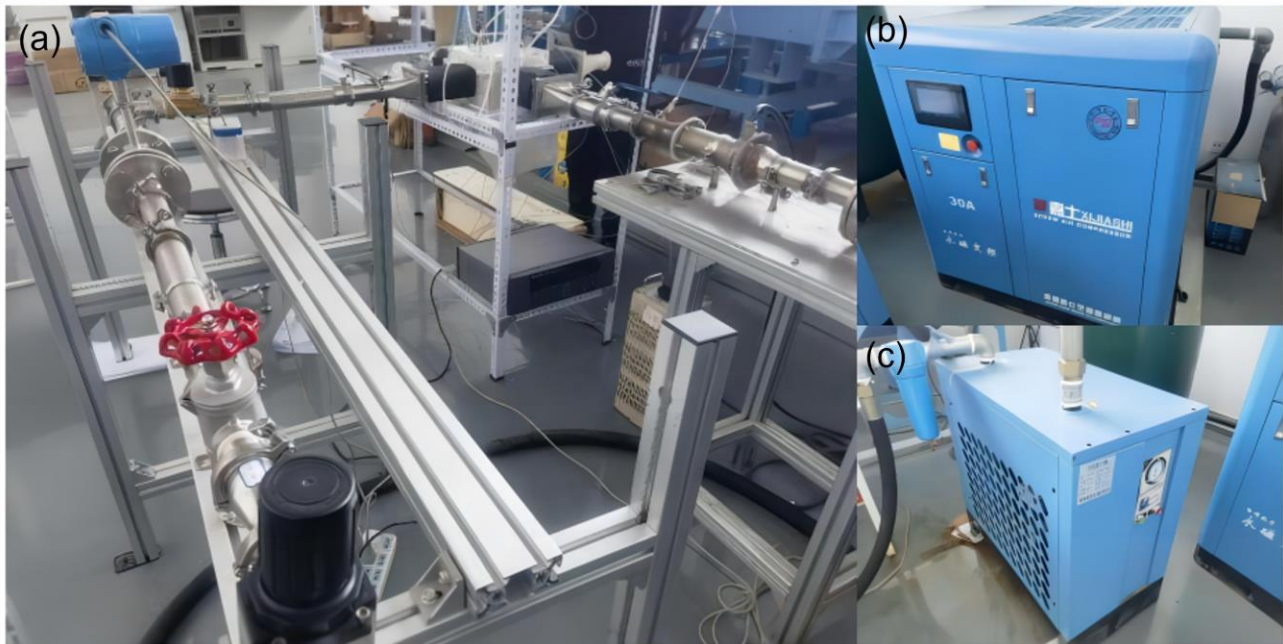
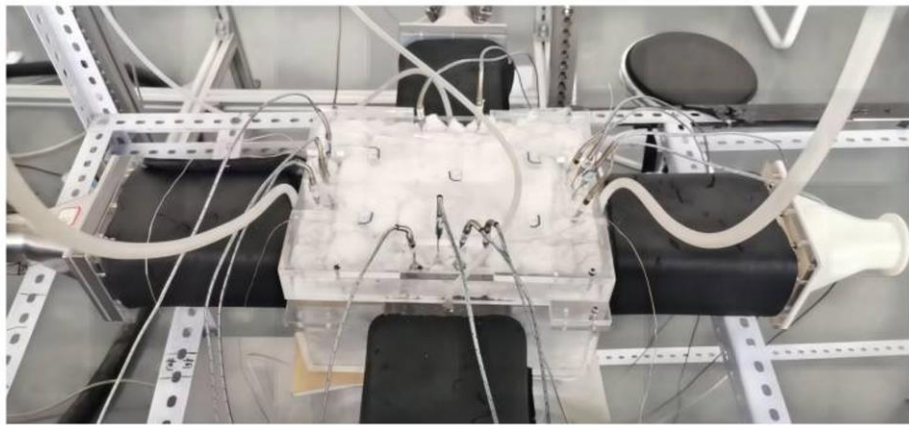


Figure 5.1. Experimental setup, (a) The overall diagram of the experimental pipeline, (b) Air compressor, (c) Air dryer.

Figure 5.2 shows the details of the HX connected to the pipe system. As shown in Figure 5.2 (a), the experimental apparatus with the TMPS HX is cruciform, which is the inlet and outlet ducts for

hot flow channel and cold flow channel respectively. The intersection of the hot and cold flow channels is the HX and also the part that needs to be replaced. The hot flow channel inlet and outlet of the HX are equipped with 3 and 4 thermocouples respectively, the cold flow channel is equipped with 2 and 4. At the same time, as shown in Figure 5.2 (b), five thermocouples are placed on the TMPS HX surface to measure temperature gradient. All thermocouples are connected to a data collector (Agilent 34980A) with a sampling rate of 0.1 Hz. Through the connection with the computer, the real-time temperature data can be obtained.

(a)



(b)

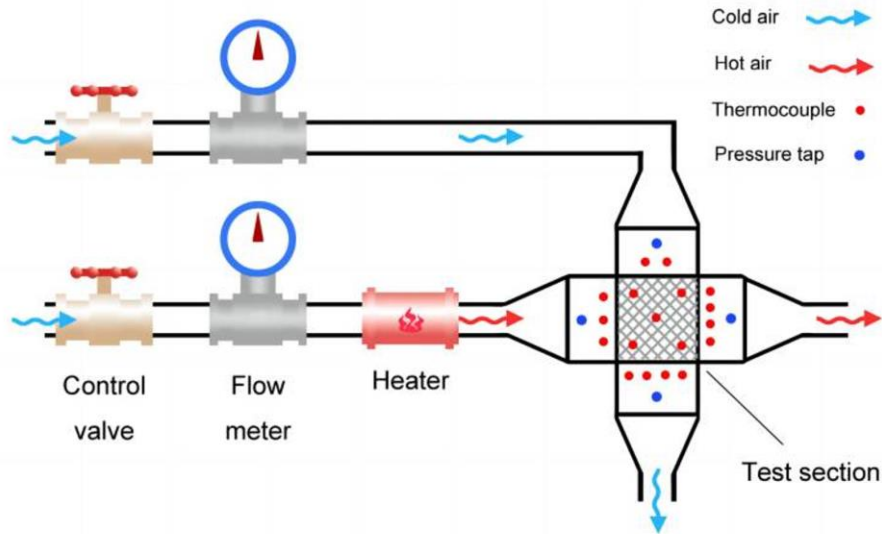


Figure 5.2. The assembly details of the experimental pipeline and HX, (a) experimental system, (b) Schematic diagram of the heat transfer experiment.

Experiments are divided into two groups, one group has a flow ratio 1:1, while the other has a flow ratio of 2:1 (hot:cold). In the experiment of 1:1 working condition, we start experiments from 20 [$m^3 h^{-1}$], gradually increase the flow rate with a step of 10 [$m^3 h^{-1}$], and recorded the data from

20-70 [$m^3 h^{-1}$]. In the flow ratio of 2:1, the hot flow rate is also 20-70 [$m^3 h^{-1}$], while the corresponding cold flow rate is 10-35 [$m^3 h^{-1}$]. It should be noted that when the measured temperature changes less than 0.2 °C within 2 minutes, it can be considered that the steady-state conditions are met. At this time, relevant data such as temperature and pressure drop can be recorded for further analysis.

5.2. Data Extraction

This experiment aims to obtain reliable data through practical measurements and compare the overall performance with the S-D HX under the same conditions. The experimental results can also verify the simulation results. The flow and heat transfer performance of the HX is determined by measuring heat transfer effectiveness and pressure drop under different flow rates (Li, Yu, and Yu 2020).

In order to make a comprehensive evaluation of the F-RD HX, heat transfer effectiveness, heat transfer coefficient, Nusselt number, Friction coefficient f and overall thermal efficiency were selected as the evaluation parameters. The Reynolds number is defined by the following formula:

$$Re = \frac{vD_h}{\nu} \quad (7)$$

Where v , D_h , ν are flow velocity, channel hydraulic diameter and kinematic viscosity respectively.

Wherein, due to the special structure of TPMS, the calculation method of waterway hydraulic diameter is (Li, Yu, and Yu 2020):

$$D_h = \frac{4 * A}{p} \quad (8)$$

Where A is the cross-section area and p is the circumference of the fluid channel.

The heat transfer effectiveness is defined by the following formula:

$$\varepsilon = \frac{Q_{avg}}{Q_{max}} \quad (9)$$

$$Q_{avg} = \frac{Q_{hot} + Q_{cold}}{2} = C_p * \dot{m} * |T_{in} - T_{out}| \quad (5)$$

Where Q , \dot{m} , C_p are heat transfer rate, mass flow rate and specific heat.

$$\varepsilon = \frac{Q_{avg}}{Q_{max}} = \frac{Q_{avg}}{(C_p * \dot{m})_{min} * (T_{hot,in} - T_{cold,in})} \quad (6)$$

Logarithmic mean temperature difference LMTD is defined by following equation,

$$LMTD = \frac{(T_{hot,in} - T_{cold,out}) - (T_{hot,out} - T_{cold,in})}{\ln(\frac{T_{hot,in} - T_{cold,out}}{T_{hot,out} - T_{cold,in}})} \quad (4)$$

Taking some of them as examples, $T_{hot,in}$ represents the fluid temperature at the inlet of the hot channels, $T_{cold,out}$ represents the fluid temperature at the outlet of the cold channels. The overall heat transfer coefficient U is

$$U = \frac{Q_{avg}}{LMTD * A * \Phi} \quad (3)$$

Where Φ is the correction coefficient, A is the average heat transfer area of hot and cold channels, which are measured by CAD software.

The correction coefficient can be determined from the Figure 5.3, where t_o, t_i, T_o, T_i are hot channel outlet temperature, hot channel inlet temperature, cold channel outlet temperature, cold channel inlet temperature.

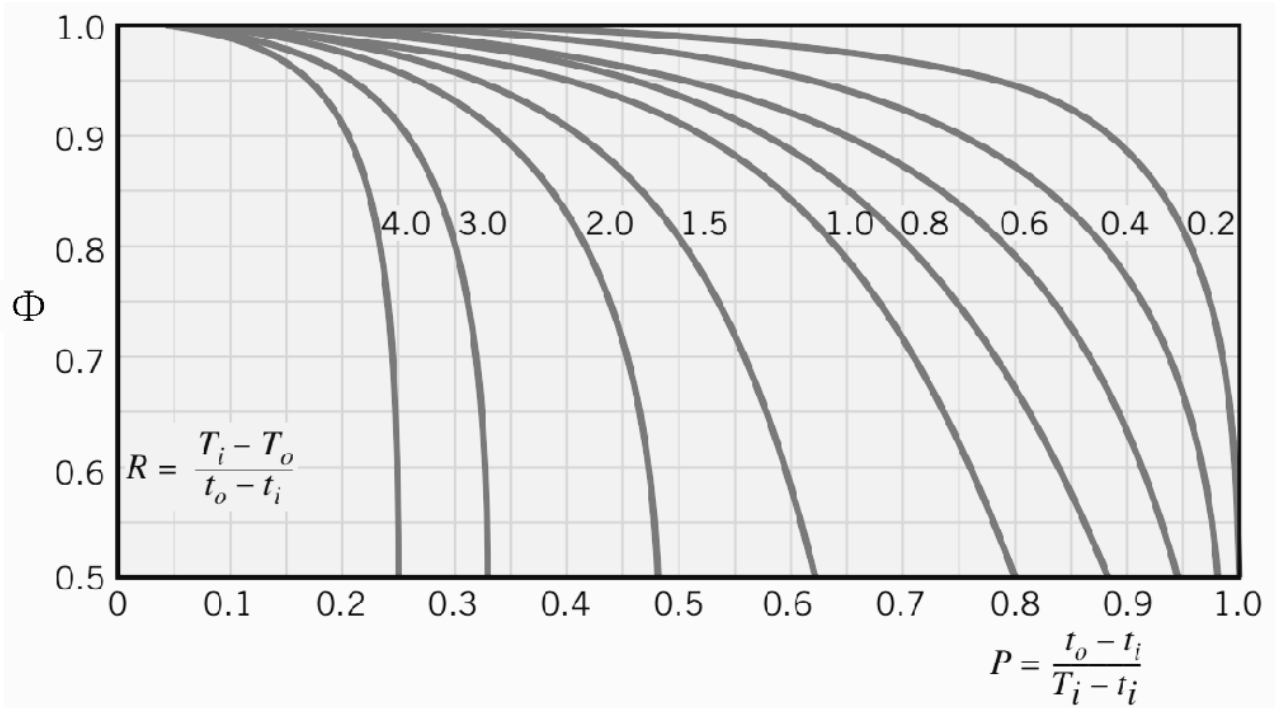


Figure 5.3. Correction factor for a single-pass, cross-flow heat exchanger with both fluids unmixed (Whitaker 2013).

The Number of Transfer Units is:

$$\text{NTU} = \frac{UA}{(C_p * \dot{m})_{min}} = \frac{Q_{avg}}{LMTD * (C_p * \dot{m})_{min}} \quad (10)$$

The physical significance of the Nusselt number is a dimensionless number indicating the intensity of heat convection:

$$Nu = \frac{h_{local} D_h}{K_f} \quad (11)$$

Wherein, D_h and k_f are the hydraulic diameter and thermal conductivity of the fluid channel.

In this experiment, the h is measured and calculated by the thermal resistance series method:

$$\frac{1}{U} = \frac{1}{h_{hot}} + \frac{t}{\lambda_{air}} + \frac{1}{h_{cold}} \quad (12)$$

Since the thermal resistance of heat conduction can be ignored, and the convective heat transfer is absolutely dominant, what needs to be determined is h_{hot} and h_{cold} . For example, $h_{hot}=h_{cold}$ in 1:1 working condition, at this time $h \approx 2U$, then the value of Nu can be calculated.

The local friction coefficient is calculated from the pressure drop at the fluid inlet and outlet:

$$f = \frac{2\Delta P}{\rho_k V_k^2} \left(\frac{D_h}{L_k} \right) \quad (13)$$

Here, ΔP 、 ρ_k 、 V_k 、 L_k are the pressure drop, the density of air, the plane average velocity at the plane k, and the length of the experimental setup.

For overall thermal efficiency η , by calculating the Nusselt number and the friction coefficient under the smooth channel:

$$f_0 = 0.316 * Re^{-0.25} \quad (14)$$

$$Nu_0 = 0.023 Re^{0.8} Pr^n \quad (15)$$

Where, $n = 0.3$ when cooling the fluid, Pr is Planck number, and Pr is taken 0.7 in this experiment.

Through these two numbers and the Nusselt number and friction coefficient calculated above, the overall thermal efficiency can be calculated by the following formula:

$$\eta = \frac{Nu/Nu_0}{(f/f_0)^{1/3}} \quad (16)$$

5.3. Uncertainty Analysis

Because there are measurement errors in the instrument during the experiment, it is necessary to extract from known measurements to estimate a possible error range. The estimation of this possible error range is an assignment called uncertainty. Uncertainty analysis is the process of identifying, quantifying, and combining error estimates. The rigor of the experiment can be improved by calculating the uncertainty.

If function F contains n arguments x_1, x_2, \dots, x_n , then the uncertainties of F can be expressed as follows (Kline 1963):

$$\delta F = \left[\sum_{i=1}^n \left(\frac{\partial F}{\partial x_i} \delta x_i \right)^2 \right]^{1/2} \quad (17)$$

Thus, the uncertainty functions of Q_{avg}, U are as follows:

$$\frac{\delta Q_{avg}}{Q_{avg}} = \left[\left(\frac{\delta m}{m} \right)^2 + \left(\frac{\sqrt{\delta T_{out}^2 + \delta T_{in}^2}}{T_{out} - T_{in}} \right)^2 \right]^{1/2} \quad (18)$$

$$\frac{\delta U}{U} = \left[\left(\frac{\delta Q_{avg}}{Q_{avg}} \right)^2 + \left(\frac{\delta LMTD}{LMTD} \right)^2 \right]^{1/2} \quad (19)$$

Similarly, for the Nusselt number, the friction coefficient and the Comprehensive heat transfer coefficient, the uncertainty function can be expressed as:

$$\frac{\delta Nu}{Nu} = \left[\left(\frac{\delta h_{local}}{h_{local}} \right)^2 + \left(\frac{\delta D_h}{D_h} \right)^2 \right]^{1/2} \quad (20)$$

$$\frac{\delta f}{f} = \left[\left(\frac{\delta v}{v} \right)^2 + \left(\frac{\delta D_h}{D_h} \right)^2 \right]^{1/2} \quad (21)$$

$$\frac{\delta \eta}{\eta} = \left[\left(\frac{\delta f}{f} \right)^2 + \left(\frac{\delta Nu}{Nu} \right)^2 \right]^{1/2} \quad (22)$$

And uncertainty related to effectiveness:

$$\frac{\delta \varepsilon}{\varepsilon} = \left[\left(\frac{\delta Q_{avg}}{Q_{avg}} \right)^2 + \left(\frac{\delta Q_{max}}{Q_{max}} \right)^2 \right]^{1/2} \quad (23)$$

In addition, according to the literature, we can calculate the uncertainty of LMTD as follows (Ahmadi and Bigham 2022),

$$\delta LMTD = \left[\left(\frac{1 - \frac{1}{R} - \ln(R)}{(\ln(R))^2} \right)^2 (\delta T_{hot,out}^2 + \delta T_{cold,in}^2) + \left(\frac{R - 1 - \ln(R)}{(\ln(R))^2} \right)^2 ((\delta T_{hot,in}^2 + \delta T_{cold,out}^2) \right]^{1/2} \quad (24)$$

$$R = \frac{T_{hot,out} - T_{cold,in}}{T_{hot,in} - T_{cold,out}} \quad (25)$$

By calculation, the uncertainty of U and Nu is approximately 4%, for ε , f and η , is about 5%, 4.5% and 3.8%. In addition, the uncertainty of pressure drop ΔP is 2%, which is determined by the accuracy of the pressure gauge.

5.4. Analyzing Experimental Results

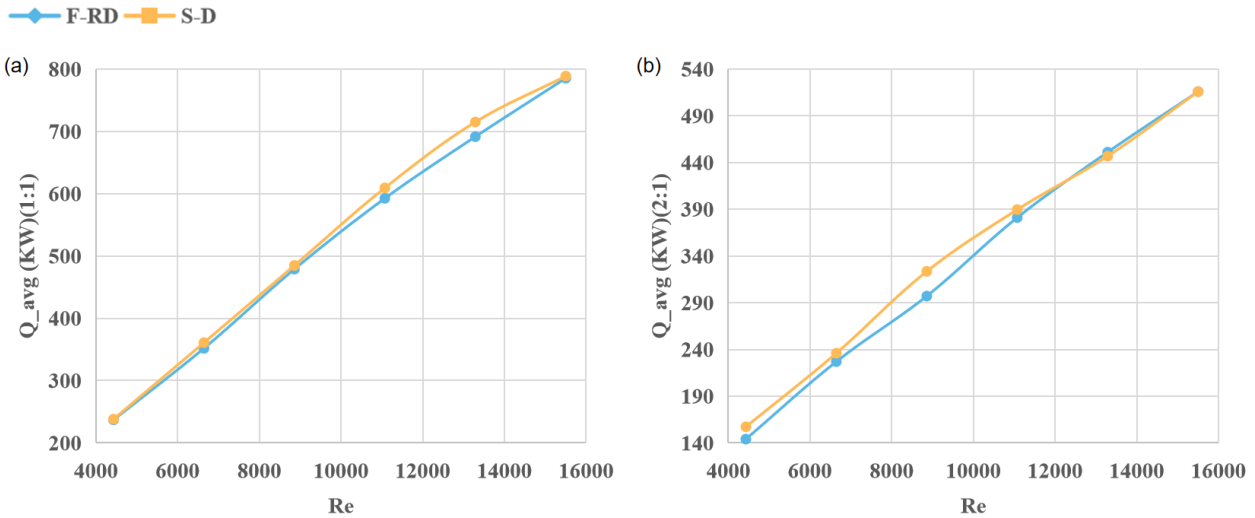


Figure 5.4. Results of the average heat exchange rate experiments, (a) $Q_{avg}(1:1)$ versus Re , (b) $Q_{avg}(2:1)$ versus Re .

Figure 5.6 (a) and (b) show the average heat exchange rate (Q_{avg}) curves of the two HXs under the two flow ratio conditions. It is not difficult to see that under different flow ratio conditions, the heat exchange rates of the F-RD HX and the S-D HX have similar sizes and trends. With the increase of Reynolds number, the flow of heat transfer gas is increasing, so it is not difficult to understand that the average heat exchange rate of the two HXs is also increasing under the two flow ratio conditions.

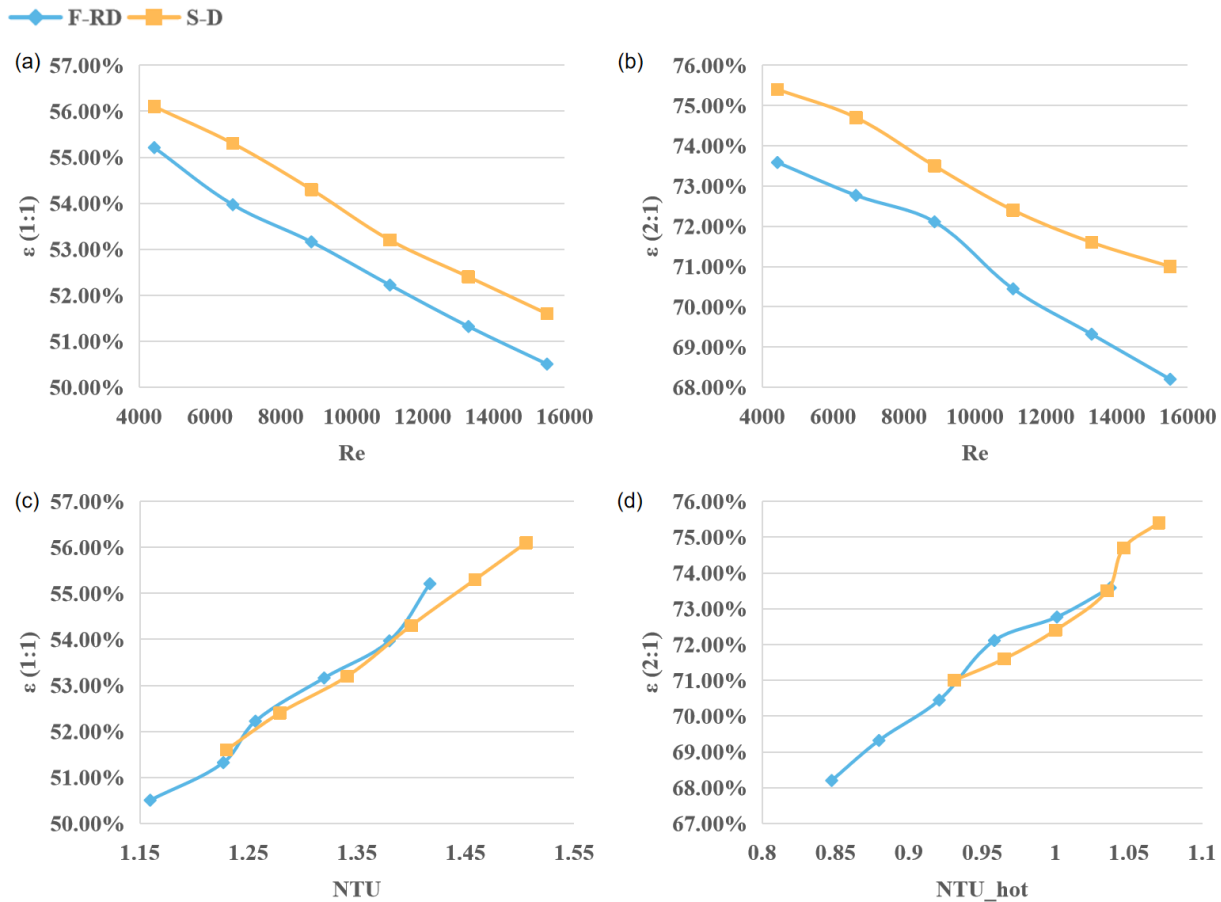


Figure 5.5. Results of the heat transfer efficiency experiments, (a) Effectiveness(1:1) versus Re , (b) Effectiveness(2:1) versus Re , (c) Effectiveness(1:1) versus NTU , (d) Effectiveness(2:1) versus NTU .

Figure 5.5 (a) and (b) show the final heat transfer effectiveness (ε) of the two HXs under the two flow ratio conditions. As shown here, with the Reynolds number as the independent variable, the final heat transfer effectiveness of the S-D HX is similar with the F-RD HX in both conditions. Meanwhile, the heat transfer effectiveness of both HX decreases as the Reynolds number increases. This is because under higher flow conditions, the residence time of the fluid is reduced. The values show that the final heat transfer effectiveness of the S-D HX is about 2% better than that of the F-RD HX in the 1:1 condition and about 4% in the 2:1 condition. In Figure 5.6 (c) and (d), when NTU_{hot} is used as the independent variable, the S-D HX have larger NTU and effectiveness values in the two flow ratio conditions. Therefore, the S-D HX has a slightly greater advantage in heat transfer.

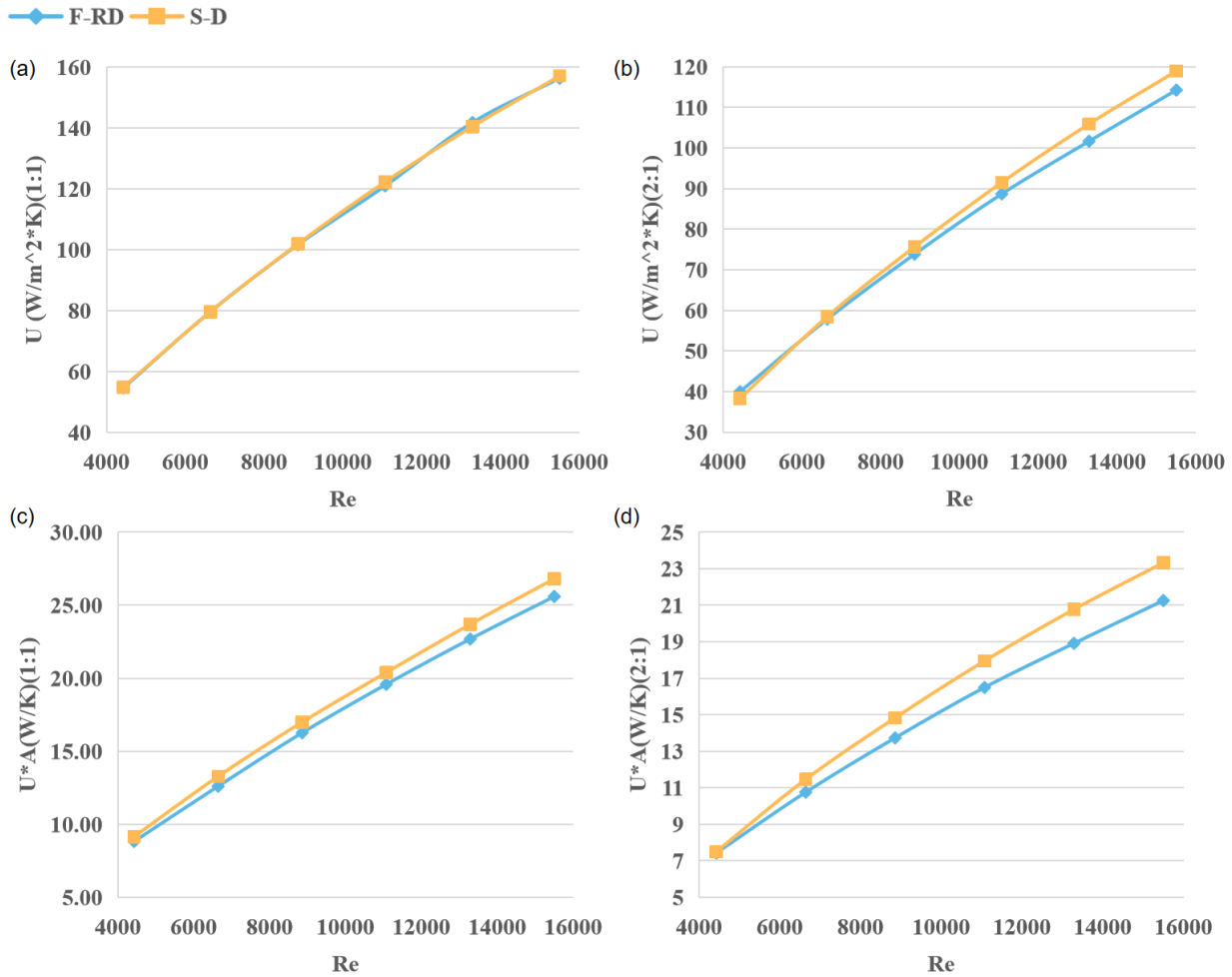


Figure 5.6. Results of the heat transfer coefficient experiments, (a) $U(1:1)$ versus Re , (b) $U(2:1)$ versus Re , (c) $U^*A(1:1)$ versus Re , (d) $U^*A(2:1)$ versus Re .

Figure 5.4 (a) and (b) show the heat transfer coefficient (U) calculated from the experimentally measured data. It can be seen that the heat transfer coefficients of the two HXs are similar in the two flow ratio conditions. This is consistent with the analysis results of the simulation section. The heat transfer coefficient increases with the increase of the flow rate. At the same time, under the 2:1 condition, the heat transfer coefficient of the S-D HX increases more with the increase of Reynolds number than that of the F-RD HX. It is worth noting that since the heat transfer area of the S-D HX is slightly larger than that of the F-RD HX, the U^*A value of the S-D HX is larger than that of the F-RD HX after multiplying the heat transfer coefficient by the corresponding area. In addition, with the increase of Reynolds number, the difference between U^*A of the two HXs is enlarged, which is more obvious in 2:1 flow ratio condition. Figure 5.4 (c) and (d).

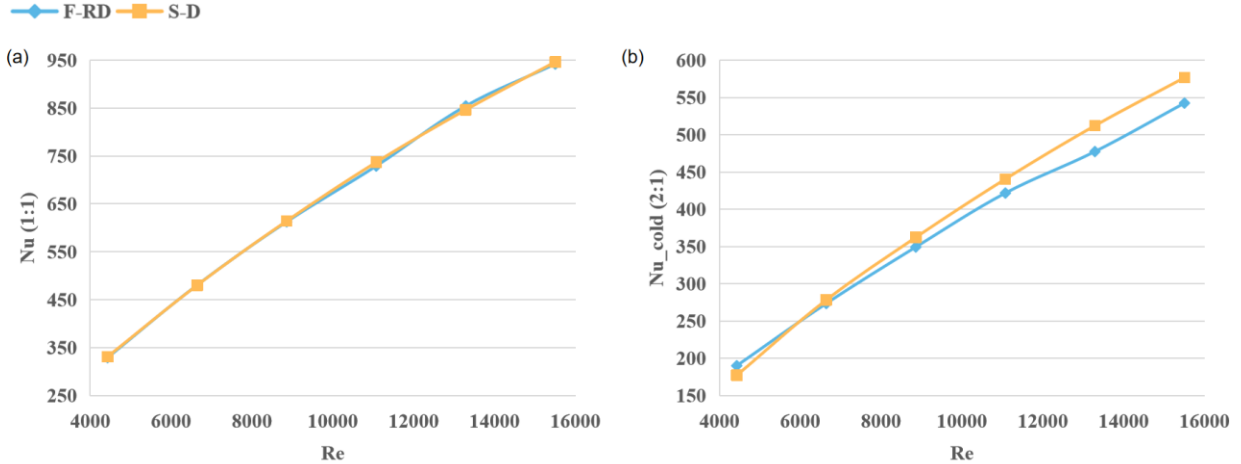


Figure 5.7. Results of the Nusselt number experiment, (a) $\text{Nu}(1:1)$ versus Re , (b) $\text{Nu}_{\text{cold}}(2:1)$ versus Re .

Figure 5.7 (a) and (b) shows the comparison diagram of Nusselt number of the two HXs under two flow ratio conditions. It is worth noting that in 2:1 flow ratio condition, h_{hot} is assumed to be constant, and then the h_{cold} is derived by the following formula to calculate Nu_{cold} .

$$\frac{1}{U} = \frac{1}{h_{\text{hot}}} + \frac{t}{\lambda_{\text{air}}} + \frac{1}{h_{\text{cold}}} \quad (26)$$

The Nusselt number of the two HXs is similar under 1:1 condition, and the Nusselt number of the S-D HX is higher than that of the F-RD HX under 2:1 condition. With the increase of Reynolds number, the gap between the two is widening. It can be concluded that the SD HX has slightly better convective heat transfer performance.

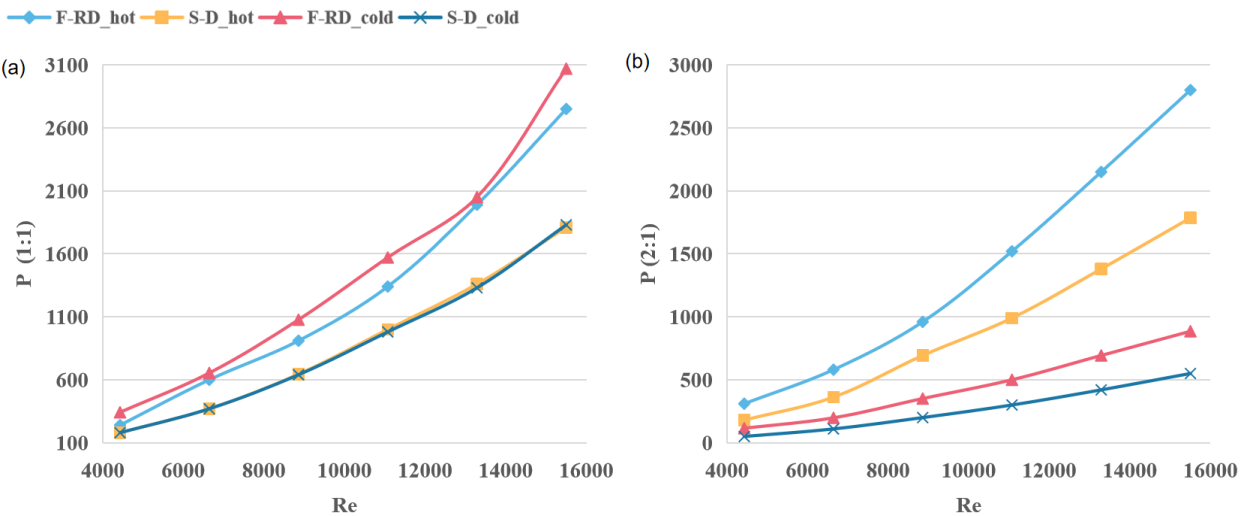


Figure 5.8. Results of pressure drop experiments, (a) pressure drop(1:1) versus Re , (b) pressure drop(2:1) versus Re .

Figure 5.8 (a) and (b) show the comparison of the pressure drop, and the pressure drop of the F-RD HX are significantly higher than that of the S-D HX. This is consistent with the analysis results of the simulation section. As the Reynolds number increases, the fluid flow increases, so the pressure drop is rising. It is worth noting that under the 1:1 working condition, cold and hot flow channels have similar pressure drop, which is consistent with the simulation results. In the F-RD HX, the pressure drop at the cold channel is significantly higher than that at the hot channel, because there is a difference in the area of blockage surface between the cold channel and the hot channel.

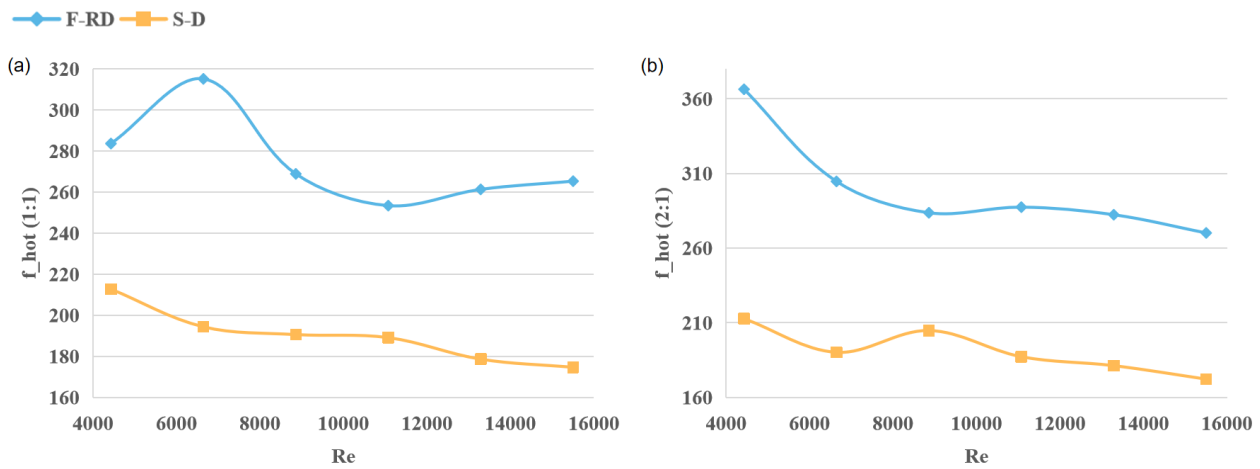


Figure 5.9. Results of friction coefficient experiments, (a) resistance coefficient(1:1) versus Re , (b) resistance coefficient(2:1) versus Re

Figure 5.9 (a) and (b) correspond to the friction coefficient(hot) between the two conditions. The friction coefficient of the F-RD HX is higher than that of the S-D HX, which is about 34% higher in the 1:1 condition and 45% higher in the 2:1 condition. In terms of pressure drop we believe that the S-D HX is better than the F-RD HX.

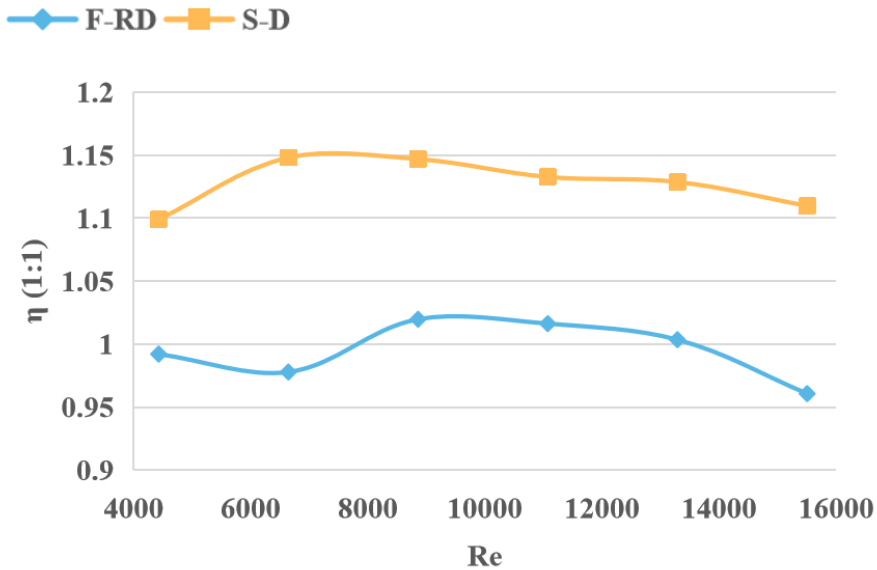


Figure 5.10. Results of overall thermal efficiency experiments, comprehensive heat transfer coefficients (1:1) versus Re .

Figure 5.10 shows the comparison of the overall thermal efficiency of the two HXs under the 1:1 flow ratio condition. The overall thermal efficiency of the S-D HX is overall higher than the F-RD HX, which is approximately 18% higher. This is mainly due to the significant difference in friction coefficient between the two HXs.

5.5. Summary of Experiment

This section introduces the relevant information of the experimental device, displays the indicators used to process experimental data, and calculates the uncertainty. Through multiple sets of experiments and processing of experimental data, the following results can be obtained: in terms of heat transfer effectiveness and heat transfer coefficient, the S-D HX and the F-RD HX are numerically similar, with the S-D HX having a few percentage weak advantage; The comparison of Nusselt number shows that the performance of the two HXs is similar, and the S-D HX has more advantages under 2:1 flow rate conditions; The values of the F-RD HX are higher than the S-D HX in terms of pressure drop and friction coefficient; The overall thermal efficiency of the S-D HX is about 18 percentage points higher than that of the F-RD HX. The comprehensive experimental results indicate that these two types of HXs have similar heat transfer performance, with the S-D HX having slight advantages. This part of the results is similar to the simulation part, which can prove the accuracy of the simulation results.

Chapter 6.

Mechanical Compression Test

In this chapter, the mechanical compression test will be carried out on the array of 3×3×3 F-RD units, and the mechanical properties of F-RD will be analyzed by comparing the test results of S-D under the same conditions. Figure 6.1 shows the equipment used for mechanical testing.

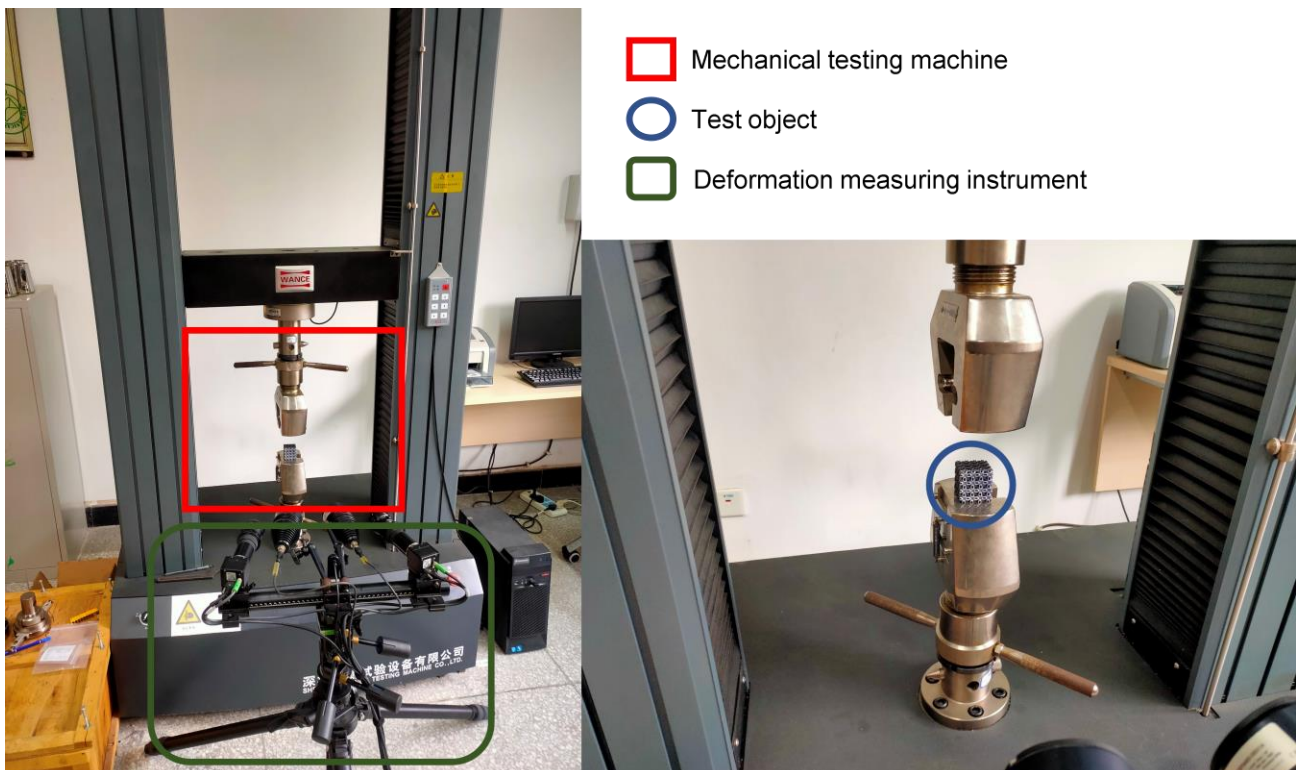


Figure 6.1. Mechanical compression test equipment.

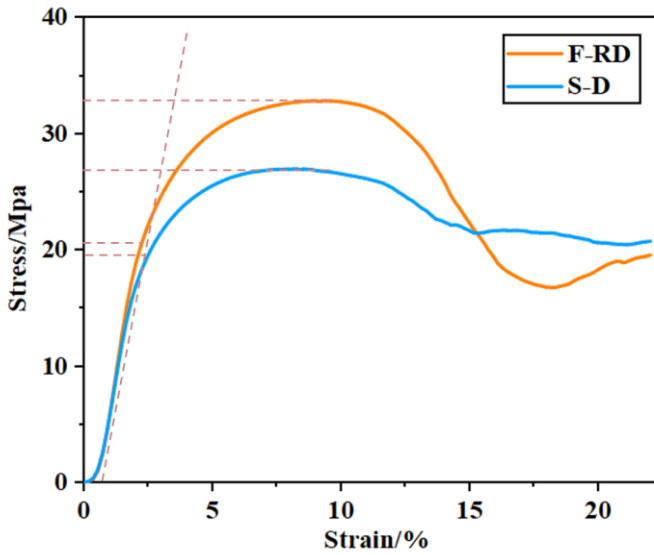


Figure 6.2. Compression test curve.

Figure 6.2 is the result of the compression test. The 0.2% offset method is used to find the corresponding yield stress, and the slope of the straight line represents the elastic modulus E, and the highest point is the maximum stress. Table 6.1 compares the relative parameters between the S-D and F-RD.

Table 6.1. Statistics of mechanical properties.

Unit	Elastic Modulus E (MPa)	Yield Stress (MPa)	Maximum Stress (MPa)
F-RD	1138	21	32.85
S-D	983	18	27

Through a comprehensive analysis of the experimental results, it can be concluded that the F-RD structure exhibits superior strength and stiffness characteristics when compared to S-D. Therefore, the F-RD structure exhibits better mechanical properties, making it suitable for applications that demand both high heat transfer performance and excellent mechanical characteristics, such as the aerospace industry.

Chapter 7.

Exploration of Hybrid-TPMS Structure

This chapter describes the method of modeling the uniform TPMS structure and H-TPMS structure. Figure 7.1 is the workflow chart that would be helpful to understand steps for generating high-precision TPMS models. Modeling processes of uniform S-D structure and L-CTG structure between G and S-D are introduced in the following sections.

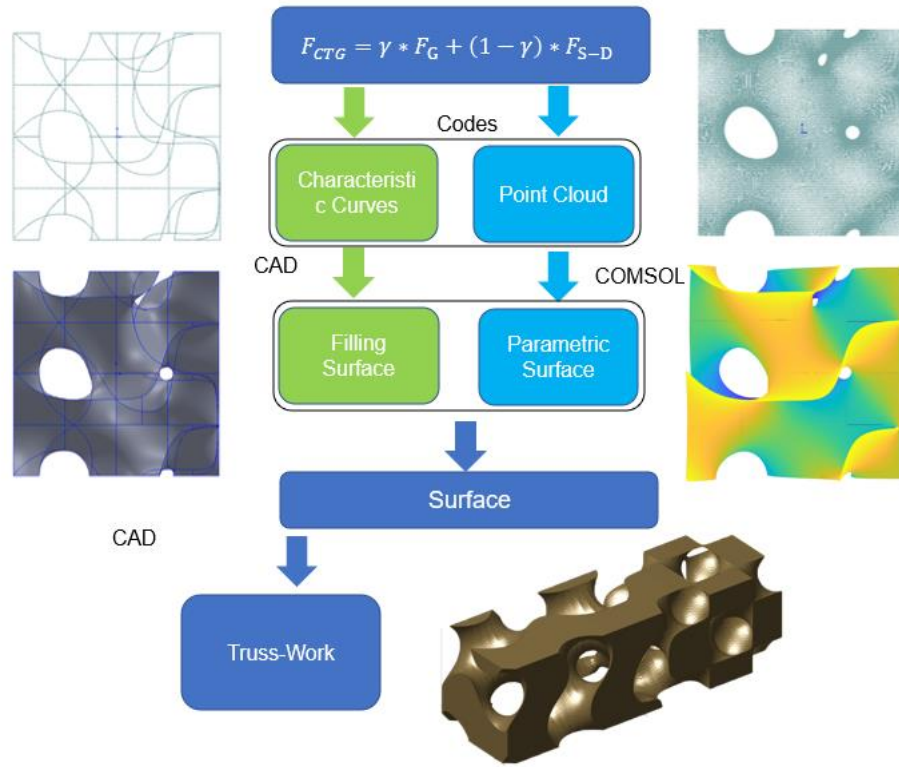


Figure 7.1. Workflow chart for L-CTG H-TPMS modeling.

7.1. Uniform TPMS Structure Modeling

Two methods to establish S-D surface are introduced, *Characteristic curves and Parameter surface*. Meantime, to model TPMS Sheet-Work structures, using surfaces $f_{S-D} = \pm 0.2$ to sandwich and form closed space is another effective method besides thickening directly in normal direction.

7.1.1. Characteristic Curves

According to S-D structure's original equation shown in Table 2.1. Set $c = 0$ and $\omega_x = \omega_y = \omega_z = 1$. Then equation for uniform S-D structure with period, also side length, of $L = \frac{2\pi}{1} = 2\pi$ is derived.

$$F_{S-D}(x, y, z) = \cos x \cos y \cos z - \sin x \sin y \sin z = 0 \quad (27)$$

Put equation $F_{S-D}(x, y, z)$ into MATLAB program, which is designed for point cloud modeling in certain 3D area. The area is limited in the domain $D = \{x \in [-\pi, \pi], y \in [-\pi, \pi], z \in [-\pi, \pi]\}$. The primary point cloud is obtained after calculations, as shown in Figure 7.2 (a). Obviously, the point cloud contains pseudo-data called noise, so it is necessary to remove the pseudo-data and noise. Figure 7.2 (b) shows the $\pi \times \pi \times \pi$ point cloud of S-D structure after denoising. The method of denoising is *Gaussian filtering*. The method is averaging the minimum distances between a certain point and corresponding other points and then removing points with excessive weight. *Gaussian filtering* is recommended because of its regulatable accuracy and high precision to maintain objectives' original appearance.

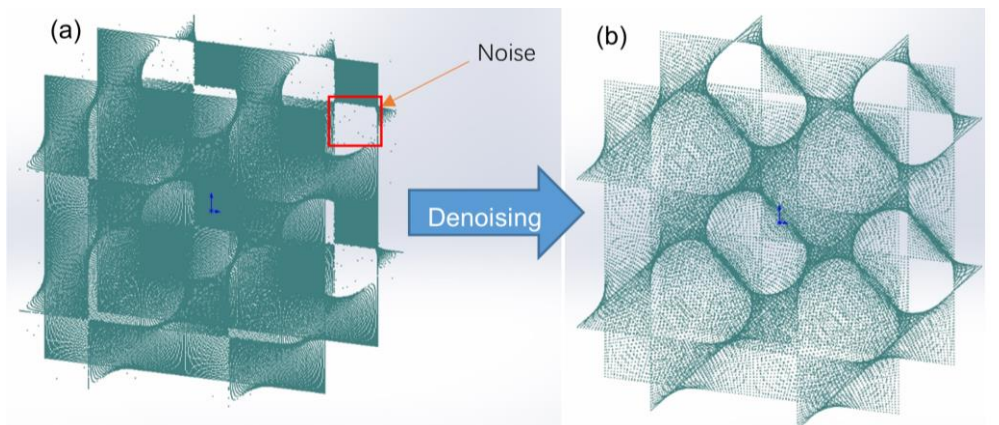


Figure 7.2. Pont cloud models, (a)Point cloud model of S-D before denoising, (b)Point Cloud Model of S-D after denoising.

Next, certain planes are used to cut the point cloud to obtain feature curves of S-D structure on these planes. Then points on each feature curve are extracted from the point cloud model in MATLAB. These points are then imported into CAD in turn to form corresponding characteristic curves. The characteristic curves of the S-D structure are showed in Figure 7.3 (a). Then, by filling the surface enclosed by the characteristic curve. S-D's high-precision surface model is obtained, as shown in Figure 7.3 (b). Then the surface is thickened directly in normal direction to model Sheet-Work S-D. Figure 7.3 (c) shows the Sheet-Work S-D structure.

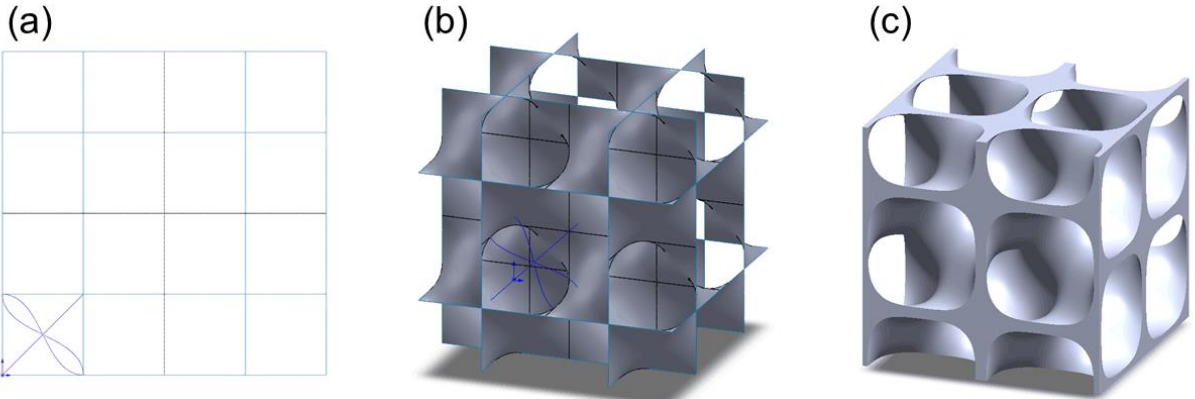


Figure 7.3. (a) Sum model of characteristic curves for S-D, (b) Surface model of S-D, (c) Sheet-Work S-D structure.

7.1.2. Parameter Surface

The surface function of uniform S-D is transformed into a function with x, y as the independent variable and z as the function of the dependent variable.

$$z = f(x, y) \quad (28)$$

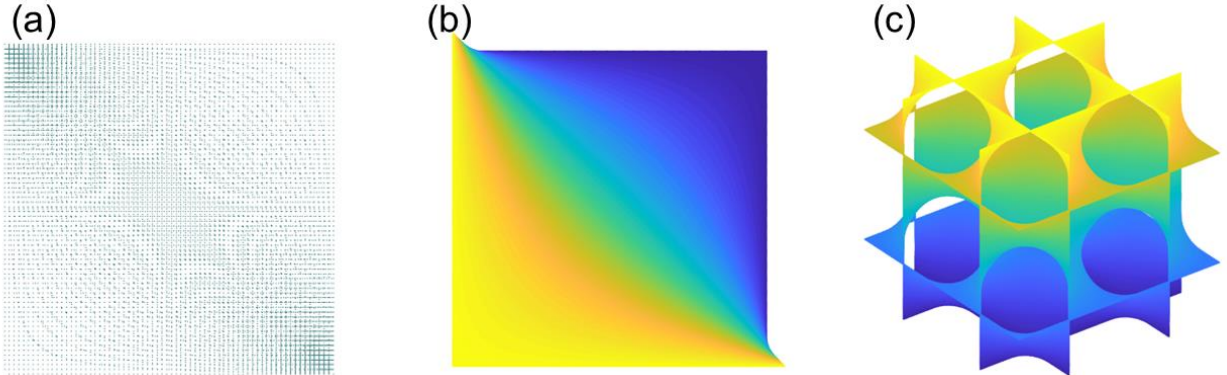


Figure 7.4. (a) Point cloud for S-D in D_1 , (b) Parameter surface for S-D in D_1 , (c) Parameter surface for S-D structure.

And it is found that there are two functions f_1 and f_2 to completely construct the S-D structure, and the corresponding point cloud model can be obtained respectively. Point Cloud for S-D is obtained in the domain $D_1 = \left\{x \in \left[\frac{3}{2}\pi, \pi\right], y \in \left[\frac{3}{2}\pi, \pi\right], z \in \left[\frac{3}{2}\pi, \pi\right]\right\}$ by MATLAB codes. Then interpolation function is derived for point cloud for S-D in D_1 , and the corresponding parameter surface is established. Next, stitch all parameter surface in $D = \{x \in [-\pi, \pi], y \in [-\pi, \pi], z \in [-\pi, \pi]\}$ to get the whole parameter surface for S-D in D . Figure 7.4 (a) shows point cloud for S-D in D_1 . Figure 7.4 (b) shows the parameter surface for S-D in D_1 . Figure 7.4 (c) shows the parameter surface for

whole S-D structure. Finally, the Sheet-Work S-D structure is built by thickening parameter surface directly in normal direction.

7.1.3. Sandwich Structure Modeling

Initially, establish surfaces $f_{S-D} = \pm 0.2$. Then fill the space sandwiched by $f_{S-D} = \pm 0.2$ to model the Sheet-Work for S-D. Figure 7.5 (a) shows surface $f_{S-D} = 0.2$. Figure 7.5 (b) shows surface $f_{S-D} = -0.2$. Figure 7.5 (c) shows sandwich Sheet-Work structure for S-D.

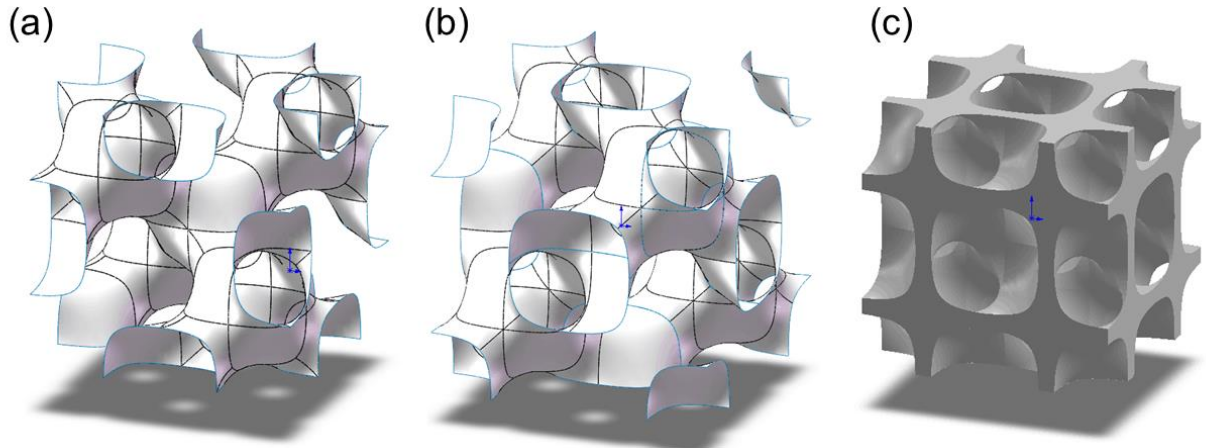


Figure 7.5. (a) Surface for $f_{S-D} = 0.2$, (b) Surface for $f_{S-D} = -0.2$, (c) Sandwich Sheet-Work structure for S-D.

7.2. H-TPMS Structure: L-CTG modeling

Since CTG is a method of combining different kinds of TPMS surfaces, the function formed should come from two function of the original structures and the transition function that exists to bridge the two functions. Suppose the transition function is γ , then the new surface function can be represented as:

$$F_{CTG} = \gamma * F_{Surface1} + (1 - \gamma) * F_{Surface2} = c \quad (29)$$

where F_{CTG} is the CTG surface function made of two surface functions, $F_{Surface1}$ and $F_{Surface2}$, and γ is a spatial weighting function with a value between 0 and 1.

$$\gamma(x, y, z) = \frac{1}{1 + e^{kG(x, y, z)}} \quad (30)$$

k is width-value of transition part of CTG structure and determines smooth degree of transition part, and $G(x, y, z)$ is shape function of transition part of CTG and dominates the shape and location of transition part.

Through the derivation of the formula, it is determined for L-CTG that the transition shape function is $G(x, y, z) = x$ and width-value is $k = 1$, which means that the transition takes place at surface $x = 0$ and is relatively gentle. Set $c = 0$ and $\omega_x = \omega_y = \omega_z = 1$. Then equation for L-CTG structure with period, also side length, of $L = \frac{2\pi}{1} = 2\pi$ is derived.

$$\begin{aligned} F_{S-D\&Gyroid} &= \gamma * F_{S-D} + (1 - \gamma) * F_{Gyroid} \\ &= \frac{1}{1 + e^x} (\sin(x)\cos(y) + \sin(y)\cos(z) + \sin(z)\cos(x)) \\ &\quad + \frac{e^x}{1 + e^x} (\cos(x)\cos(y)\cos(z) - \sin(x)\sin(y)\sin(z)) = c \end{aligned} \quad (31)$$

According to its original formula ($F_{S-D\&Gyroid} = 0$), the characteristic curves model for L-CTG structure between G and S-D is obtained through MATLAB codes. Then fill and stitch surfaces to establish the surface model of $F_{S-D\&Gyroid} = 0$. Then fill the space that satisfies $F_{S-D\&Gyroid} > 0$ to finish the Solid-Work model for L-CTG. Figure 7.6 (a) is the characteristic curves for L-CTG structure between Gyroid and S-D. Figure 7.6 (b) is the surface model for L-CTG structure between G and S-D. Then the Solid-Work hybrid model is generated, as shown in Figure 7.6 (c).

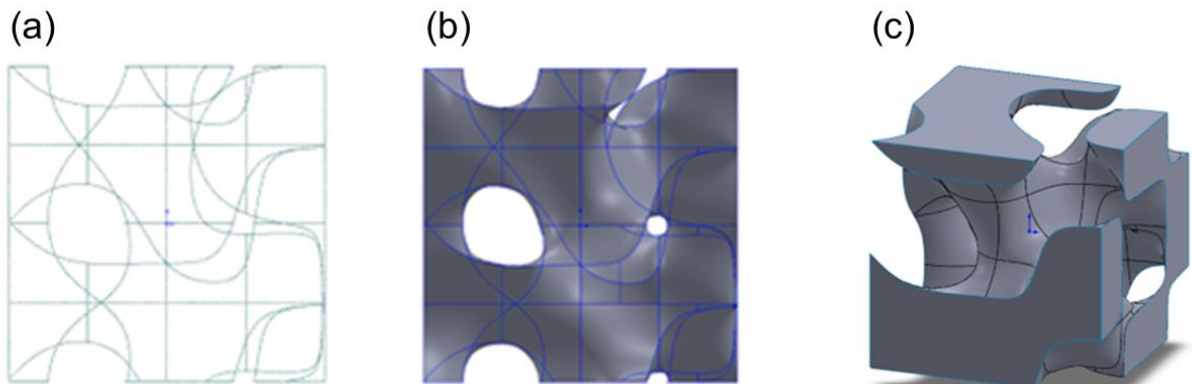


Figure 7.6. (a) Characteristic curves of Transition of Gyroid to S-D, (b) Surface of Transition of Gyroid to S-D, (c) Solid-Work for L-CTG structure between Gyroid and S-D in domain D.

Adding S-D and G structures to transition part, it is obvious that G structure and S-D structure are successfully connected. Figure 7.7 is the Truss-Work for L-CTG structure for Gyroid and S-D.

For transition part of L-CTG structure, the excessive variation in curvature resulted in inapplicability of the thickening operation. Through trials, it is found that using sandwich modeling to build the Sheet-Work model of L-CTG structure is feasible.



Figure 7.7. Truss-Work for L-CTG structure between Gyroid and S-D in domain D_2 .

Based on surfaces $F_{S-D\&Gyroid} = \pm 0.2$, fill in the solids between two surfaces in CAD to build the Sheet-Network model. Figure 7.8 (a) is the surface $F_{S-D\&Gyroid} = 0.2$. Figure 7.8 (b) is the surface $F_{S-D\&Gyroid} = -0.2$. Figure 7.8 (c) shows two surfaces in CAD, which is clearer to express sandwich modeling. Figure 7.8 (d) is the final sandwich Sheet-Work for L-CTG structure between G and S-D.

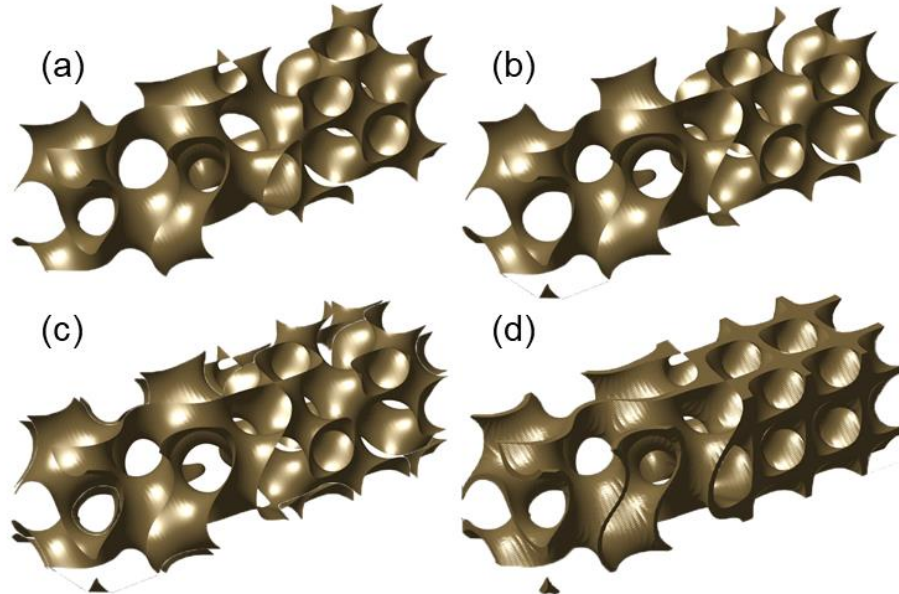


Figure 7.8. (a) Surface $F_{S-D\&Gyroid} = 0.2$, (b) Surface $F_{S-D\&Gyroid} = -0.2$, (c) Sandwich expression for L-CTG, (d) Sheet-Work for L-CTG structure between G and S-D.

Chapter 8.

Conclusion and Future Works

8.1. Conclusion

Firstly, this study presents the whole process of designing and manufacturing the F-RD HX, evaluating the manufacturing process through SEM experiments, and proposing optimization strategies, it is found to achieve the desired porosity, an appropriate reduction in wall thickness should be made during the design stage. Because during the SLM manufacturing process, melting occurs causing the metal to adhere to the metal powder, and molten metal to flow laterally, which result in a larger wall thickness than intended. Based on the comparative data presented in Table 3.2, it can be concluded that SLM manufacturing technology offers higher precision overall. However, it is important to note that the resulting surface may have a certain level of roughness. To mitigate the potential impact of friction on the HX and optimize heat transfer performance, a specific post-treatment process can be implemented, such as polishing the surface. This post-treatment process helps to reduce surface roughness, and prolong the service life of the HX and enhance the overall performance of the HX.

Then, this study conducts numerical simulations of the F-RD and S-D HXs using simplified models, and compares the heat transfer characteristics and flow mechanisms within them. The F-RD and S-D HXs demonstrate similar overall heat transfer performance, but exhibit significant differences in terms of flow mechanisms. Unlike most TPMS structures, the F-RD HX does not induce obvious three-dimensional flow pattern and mainly enhances heat transfer through the impingement of the fluid and solid wall. On the other hand, the S-D HX relies on large-scale three-dimensional flow and numerous bifurcated flows to enhance heat transfer, and the diagonal flow of the fluid increases the heat transfer path, which also increases the heat transfer to some extent. In terms of pressure drop, both the cold and hot channels of the S-D heat exchanger have similar blockage areas, and its internal units are symmetrically, resulting in similar pressure drops for both hot and cold flows. The pressure drops in S-D HX are smaller than that of the F-RD HX. The F-RDHX has significant differences in the blocked areas of its hot and cold channels, resulting in different pressure drops for each channel. Additionally, due to the impingement heat transfer type of the F-RD HX, it is obvious that this will result in a larger pressure drop in F-RD HX than in S-D HX.

Afterwards, heat transfer experiments are conducted on the F-RD HX, and the results of the experiments are similar to the simulation results. On the basis of simulation, indicators such as heat transfer efficiency, Nusselt number, friction coefficient, and overall thermal efficiency are calculated, and their results are consistent, specifically, both the F-RD HX and the S-D HX demonstrate similar overall heat transfer performance, and the pressure drop of both hot and cold channels matches the numerical simulation analysis, which indicates that the experimental operation and numerical simulation are reliable.

Finally, the modeling method of H-TPMS structure is explored, which is divided into two parts: the uniform TPMS structure and the H-TPMS structure. In the modeling process of the uniform TPMS structure, this research introduces two methods to establish the S-D surface: characteristic curves and parameter surface. Meantime, to model Sheet-Work for TPMS structures based on surface model, surface $F_{S-D}(x, y, z) = 0$ is directly thickened or surfaces $F_{S-D}(x, y, z) = \pm 0.2$ are used to sandwich the Sheet-Work. In H-TPMS structure (L-CTG) modeling process, the method Characteristic curves is used to build surface $F_{L-CTG}(x, y, z) = 0$, and Truss-Work for L-CTG is completed by filling space that satisfies $F_{L-CTG} > 0$. Eventually, the hybrid of G and S-D type is realized.

8.2. Future Works

Focusing on new units can contribute to the development of high-performance heat exchangers and provide valuable insights for their design. In the numerical simulation part, full-model simulation is not possible due to some limitations, resulting in the loss of some information in the numerical simulation. As a result, it is not possible to make a comprehensive comparison with the experimental results. If there are sufficient conditions, in subsequent studies, a full model simulation should be conducted by directly performing numerical simulation on the whole HX model shown in Figure 3.1. The simulation results can then be compared with the experimental results to obtain more convincing verification.

This study proposes an innovative H-TPMS modeling method, which is stuck at the stage of linking G and S-D units to form the L-CTG structure due to time constraints. This research provides a foundation for further exploration and investigation. In the future, this research can be carried out from following direction:

- Explore how to compose the structure into the HX frame;

- Conduct the numerical simulation and heat transfer experiment to evaluate the heat transfer performance;
- Explore the modeling method of other hybrid unit groups if performance improvements are observed.

References

- Aboulkhair, Nesma T., Marco Simonelli, Luke Parry, Ian Ashcroft, Christopher Tuck, and Richard Hague. 2019. '3D printing of Aluminium alloys: Additive Manufacturing of Aluminium alloys using selective laser melting', *Progress in Materials Science*, 106: 100578.
- Agarwal, Abhishek. 2021. 'Modelling and numerical investigation of the effectiveness of plate heat exchanger for cooling engine oil using ANSYS CFX', *Int J Heat Technol*, 39: 653-58.
- Ahmadi, Behzad, and Sajjad Bigham. 2022. 'Performance evaluation of hi-k lung-inspired 3D-printed polymer heat exchangers', *Applied Thermal Engineering*, 204: 117993.
- Al-Ketan, O., M. Ali, M. Khalil, R. Rowshan, and Rka Al-Rub. 2020. 'Forced convection CFD analysis of architected and 3D printable heat sinks based on triply periodic minimal surfaces', *Journal of Thermal Science and Engineering Applications*, 13: 1-33.
- Al - Ketan, Oraib, and Rashid K Abu Al - Rub. 2021. 'MSLattice: A free software for generating uniform and graded lattices based on triply periodic minimal surfaces', *Material Design & Processing Communications*, 3: e205.
- Alshaer, Ahmad W, and Daniel J Harland. 2021. 'An investigation of the strength and stiffness of weight-saving sandwich beams with CFRP face sheets and seven 3D printed cores', *Composite Structures*, 257: 113391.
- Bai, Zhenpeng, Yanfeng Li, Jin Zhang, Alan Fewkes, and Hua Zhong. 2021. 'Research on the design and application of capillary heat exchangers for heat pumps in coastal areas', *Building Services Engineering Research and Technology*, 42: 333-48.
- Bajic, S. 2019. "Analysis of the Influence of Parts of a Heat Exchanger on the Current and Temperature Fields in the Heat Exchanger Using CFD." In *18th Conference on Power System Engineering, Thermodynamics and Fluid Mechanics*. Univ W Bohemia Pilsen, Fac Mech Engn, Dept Power Syst Engn, Pilsen, CZECH REPUBLIC.
- Bobbert, F. S. L., K. Lietaert, A. A. Eftekhari, B. Pouran, S. M. Ahmadi, H. Weinans, and A. A. Zadpoor. 2017. 'Additively manufactured metallic porous biomaterials based on minimal surfaces: A unique combination of topological, mechanical, and mass transport properties', *Acta biomaterialia*, 53: 572-84.
- Cheng, Zhilong, Ruina Xu, and Pei-Xue Jiang. 2021. 'Morphology, flow and heat transfer in triply periodic minimal surface based porous structures', *International Journal of Heat and Mass Transfer*, 170: 120902.
- Delda, Ray Noel Medina, Rex Balisalisa Basuel, Rodel Peralta Hacla, Dan William Carpiano Martinez, John-John Cabibihan, and John Ryan Cortez Dizon. 2021. '3D Printing Polymeric Materials for Robots with Embedded Systems', *Technologies*, 9: 82.
- Elsheikh, Ammar H, Hitesh N Panchal, Shanmugan Sengottain, Naser A. Alsaleh, and Mahmoud Ahmadein. 2022. 'Applications of Heat Exchanger in Solar Desalination: Current Issues and Future Challenges', *Water*, 14: 852.
- Feng, Jiawei, Jianzhong Fu, Ce Shang, Zhiwei Lin, and Bin Li. 2018. 'Porous scaffold design by solid T-splines and triply periodic minimal surfaces', *Computer Methods in Applied Mechanics and Engineering*, 336: 333-52.
- Feng, Jiawei, Bo Liu, Zhiwei Lin, and Jianzhong Fu. 2021. 'Isotropic porous structure design methods based on triply periodic minimal surfaces', *Materials & Design*, 210: 110050.
- Jafari, Davoud, and Wessel W. Wits. 2018. 'The utilization of selective laser melting technology on heat transfer devices for thermal energy conversion applications: A review', *Renewable and Sustainable Energy Reviews*, 91: 420-42.
- Kapfer, Sebastian C, Stephen T Hyde, Klaus Mecke, Christoph H Arns, and Gerd E Schröder-Turk. 2011. 'Minimal surface scaffold designs for tissue engineering', *Biomaterials*, 32: 6875-82.

- Kim, Jiho, and Dong-Jin Yoo. 2020. '3D printed compact heat exchangers with mathematically defined core structures', *Journal of Computational Design and Engineering*, 7: 527-50.
- Kline, Stephen J. 1963. 'Describing uncertainties in single-sample experiments', *Mech. Eng.*, 75: 3-8.
- Kumar, Sumit, Vikram Khanna, Balendra Pratap Singh, Ranjitkumar Patil, and Divya Mehrotra. 2021. 'Purview of 3D printing in medical applications during COVID-19', *Health Policy and Technology*, 10: 25.
- Lee, Dong-Wook, Kamran A Khan, and Rashid K Abu Al-Rub. 2017. 'Stiffness and yield strength of architected foams based on the Schwarz Primitive triply periodic minimal surface', *International Journal of Plasticity*, 95: 1-20.
- Lei, Hong-Yuan, Jing-Rong Li, Qing-Hui Wang, Zhi-Jia Xu, Wei Zhou, Chang-Lin Yu, and Tian-Qing Zheng. 2019. 'Feasibility of preparing additive manufactured porous stainless steel felts with mathematical micro pore structure as novel catalyst support for hydrogen production via methanol steam reforming', *International Journal of Hydrogen Energy*, 44: 24782-91.
- Lesmana, Luthfan Adhy, and Muhammad Aziz. 2022. 'Mechanical Behaviour and Fluid Dynamics Analysis of Metal Hydride for Hydrogen Storage Based on Triply Periodic Minimal Surface Structure', *Chemical Engineering Transactions*, 94: 901-06.
- Li, Weihong, Guopeng Yu, and Zhibin Yu. 2020. 'Bioinspired heat exchangers based on triply periodic minimal surfaces for supercritical CO₂ cycles', *Applied Thermal Engineering*, 179: 115686.
- Li, Wenguang, Weihong Li, and Zhibin Yu. 2022. 'Heat transfer enhancement of water-cooled triply periodic minimal surface heat exchangers', *Applied Thermal Engineering*, 217: 119198.
- Liang, Dong, Chenwei Shi, Weihong Li, Wei Chen, and Minking K Chyu. 2023. 'Design, flow characteristics and performance evaluation of bioinspired heat exchangers based on triply periodic minimal surfaces', *International Journal of Heat and Mass Transfer*, 201: 123620.
- Liu, Fei, Zhongfa Mao, Peng Zhang, David Z Zhang, Junjie Jiang, and Zhibo Ma. 2018. 'Functionally graded porous scaffolds in multiple patterns: New design method, physical and mechanical properties', *Materials & Design*, 160: 849-60.
- Liu, Peiqing, and Peiqing Liu. 2021. 'Computational Fluid Dynamics', *A General Theory of Fluid Mechanics*: 297-332.
- Lu, Peipei, Meiping Wu, Xin Liu, Weipeng Duan, and Jitai Han. 2020. 'Study on corrosion resistance and bio-tribological behavior of porous structure based on the SLM manufactured medical Ti6Al4V', *Metals and Materials International*, 26: 1182-91.
- Mekki, Bashir S, Joshua Langer, and Stephen Lynch. 2021. 'Genetic algorithm based topology optimization of heat exchanger fins used in aerospace applications', *International Journal of Heat and Mass Transfer*, 170: 121002.
- Melchels, Ferry PW, Ana MC Barradas, Clemens A Van Blitterswijk, Jan De Boer, Jan Feijen, and Dirk W Grijpma. 2010. 'Effects of the architecture of tissue engineering scaffolds on cell seeding and culturing', *Acta biomaterialia*, 6: 4208-17.
- Murr, Lawrence E. 2019. 'Strategies for creating living, additively manufactured, open-cellular metal and alloy implants by promoting osseointegration, osteoinduction and vascularization: An overview', *Journal of Materials Science & Technology*, 35: 231-41.
- Norton, Tomás, and Da-Wen Sun. 2006. 'Computational fluid dynamics (CFD)–an effective and efficient design and analysis tool for the food industry: a review', *Trends in Food Science & Technology*, 17: 600-20.
- Padmanabhan, S, Obulareddy Yuvatejeswar Reddy, Kanta Venkata Ajith Kumar Yadav, VK Bupesh Raja, and K Palanikumar. 2021. 'Heat transfer analysis of double tube heat exchanger with helical inserts', *Materials Today: Proceedings*, 46: 3588-95.
- Ponnusamy, P., R. A. Rahman Rashid, S. H. Masood, D. Ruan, and S. Palanisamy. 2020. 'Mechanical Properties of SLM-Printed Aluminium Alloys: A Review', *Materials (Basel)*, 13.

- Qin, Ruqiong, and Chunyi Duan. 2017. "The principle and applications of Bernoulli equation." In *Journal of Physics: Conference Series*, 012038. IOP Publishing.
- Redondo, Edurne, and Martin Pumera. 2021. 'MXene-functionalised 3D-printed electrodes for electrochemical capacitors', *Electrochemistry Communications*, 124: 106920.
- Reynolds, Benjamin Wynne, Conan J Fee, Ken Morison, and Daniel J Holland. 'Characterisation of Heat Transfer within 3d Printed Tpms Heat Exchangers', Available at SSRN 4241475.
- Wang, Su, Linlin Liu, Xin Zhou, Luchuang Zhu, and Yongqiang Hao. 2020. 'The design of Ti6Al4V Primitive surface structure with symmetrical gradient of pore size in biomimetic bone scaffold', *Materials & Design*, 193: 108830.
- Whitaker, Stephen. 2013. *Fundamental principles of heat transfer* (Elsevier).
- Wu, Helong, Jie Yang, and Sritawat Kitipornchai. 2020. 'Mechanical analysis of functionally graded porous structures: A review', *International Journal of Structural Stability and Dynamics*, 20: 2041015.
- Xie, Liyi, Dawei Zhuang, Zhiqiang Li, and Guoliang Ding. 2022. 'Technical Characteristics and Development Trend of Printed Circuit Heat Exchanger Applied in Floating Liquefied Natural Gas', *Frontiers in Energy Research*, 10: 383.
- Yang, Yang, Xuan Song, Xiangjia Li, Zeyu Chen, Chi Zhou, Qifa Zhou, and Yong Chen. 2018. 'Recent progress in biomimetic additive manufacturing technology: from materials to functional structures', *Advanced Materials*, 30: 1706539.
- Yap, C. Y., C. K. Chua, Z. L. Dong, Z. H. Liu, D. Q. Zhang, L. E. Loh, and S. L. Sing. 2015. 'Review of selective laser melting: Materials and applications', *Applied Physics Reviews*, 2.
- Yeo, Seon Ju, Min Jun Oh, and Pil J Yoo. 2019. 'Structurally controlled cellular architectures for high - performance ultra - lightweight materials', *Advanced Materials*, 31: 1803670.
- Zhang, Jinliang, Bo Song, Qingsong Wei, Dave Bourell, and Yusheng Shi. 2019. 'A review of selective laser melting of aluminum alloys: Processing, microstructure, property and developing trends', *Journal of Materials Science & Technology*, 35: 270-84.
- Zhang, Xinyue. 2019. 'Design method and performance study of SLM formed sandwich structures based on triply periodic minimal surfaces (Chinese)', Chongqing University.
- Zhao, LH, RZ Wang, and TS Ge. 2021. 'Desiccant coated heat exchanger and its applications', *International Journal of Refrigeration*, 130: 217-32.

Appendix A.

H-TPMS Modeling Code

Code name: Main_Program_trial language: Matlab

```
%%
clear;clc;close all;

%%
%Definition of lattices' Functions

% F_G='sin(x)*cos(y)+sin(y)*cos(z)+sin(z)*cos(x)'; %Function of G(pi/3)*yroid

F_SD='cos(x)*cos(y)*cos(z)-sin(x)*sin(y)*sin(z)'; %Function of S_D

% F_P='cos(x)+cos(y)+cos(z)'; %Function of Primitive

% F_FRD='4*cos(x)*cos(y)*cos(z)-
(cos(2*x)*cos(2*y)+cos(2*y)*cos(2*z)+cos(2*z)*cos(2*x))'; %Function of F_RD

%%
%Solution of z_functions of Lattices

% Z_Gyroid=LatticeF(F_G); %zFunction of Gyroid

Z_SD=LatticeF(F_SD); %zFunction of S_D

% Z_Primitive=LatticeF(F_P); %zFunction of Primitive

% Z_F_RD=LatticeF(F_FRD); %zFunction of F_RD
```

```

%%

%Pretreatment of z-function: sym-char &then put'.' before '*' & '/'

% CHARFunctionZ_G1=vectorize(char(Z_Gyroid(1)));

% CHARFunctionZ_G2=vectorize(char(Z_Gyroid(2)));


CHARFunctionZ_S_D1=vectorize(char(Z_S_D(1)));

CHARFunctionZ_S_D2=vectorize(char(Z_S_D(2)));


% CHARFunctionZ_P1=vectorize(char(Z_Primitive(1)));

% CHARFunctionZ_P2=vectorize(char(Z_Primitive(2)));


%


% CHARFunctionZ_F_RD1=vectorize(char(Z_F_RD(1)));

% CHARFunctionZ_F_RD2=vectorize(char(Z_F_RD(2)));

% CHARFunctionZ_F_RD3=vectorize(char(Z_F_RD(3)));

% CHARFunctionZ_F_RD4=vectorize(char(Z_F_RD(4)));


%%

%coordinates

[X,Y] = meshgrid(-6:0.05:-3,-6:0.05:-3);

x=pi./6.*X;y=pi./6.*Y;

% eval(['zG_1=6./pi.*real('CHARFunctionZ_G1,')']);%assign to zG1

```

```

% eval(['zG_2=6./pi.*real('CHARFunctionZ_G2,');']);%assign to zG2

eval(['zSD_1=6./pi.*real('CHARFunctionZ_S_D1,');']);%assign to zSD1

eval(['zSD_2=6./pi.*real('CHARFunctionZ_S_D2,');']);%assign to zSD2

% eval(['zP_1=6./pi.*real('CHARFunctionZ_P1,');']);%assign to zP1

% eval(['zP_2=6./pi.*real('CHARFunctionZ_P2,');']);%assign to zP2

%

% eval(['zFRD_1=6./pi.*real('CHARFunctionZ_F_RD1,');']);%assign to zFRD1

% eval(['zFRD_2=6./pi.*real('CHARFunctionZ_F_RD2,');']);%assign to zFRD2

% eval(['zFRD_3=6./pi.*real('CHARFunctionZ_F_RD3,');']);%assign to zFRD3

% eval(['zFRD_4=6./pi.*real('CHARFunctionZ_F_RD4,');']);%assign to zFRD4

%Point cloud of types-TPMS

% pC_zG_1=PointCloud(pCloudF(X,Y,zG_1));

% pC_zG_2=PointCloud(pCloudF(X,Y,zG_2));

pC_zSD_1=PointCloud(pCloudF(X,Y,zSD_1));

pC_zSD_2=PointCloud(pCloudF(X,Y,zSD_2));

PCCC=[pCloudF(X,Y,zSD_1);pCloudF(X,Y,zSD_2)];

writematrix(PCCC,'S_Diamond_noise.txt','Delimiter', ' ')

```

```

% pC_zP_1=PointCloud(pCloudF(X,Y,zP_1));

% pC_zP_2=PointCloud(pCloudF(X,Y,zP_2));

rrrr = -6 + (6+6)*rand([790 3]);

% pC_zFRD_1=PointCloud(pCloudF(X,Y,zFRD_1));

% pC_zFRD_2=PointCloud(pCloudF(X,Y,zFRD_2));

% pC_zFRD_3=PointCloud(pCloudF(X,Y,zFRD_3));

% pC_zFRD_4=PointCloud(pCloudF(X,Y,zFRD_4));

% %denoising

% [P_zG1,zG1]=denoisingcloudF(X,Y,zG_1);

% [P_zG2,zG2]=denoisingcloudF(X,Y,zG_2);

%

% [P_zSD1,zSD1]=denoisingcloudF(X,Y,zSD_1);

% [P_zSD2,zSD2]=denoisingcloudF(X,Y,zSD_2);

%

% [P_zP1,zP1]=denoisingcloudF(X,Y,zP_1);

% [P_zP2,zP2]=denoisingcloudF(X,Y,zP_2);

%

% [P_zFRD1,zFRD1]=denoisingcloudF(X,Y,zFRD_1);

% [P_zFRD2,zFRD2]=denoisingcloudF(X,Y,zFRD_2);

% [P_zFRD3,zFRD3]=denoisingcloudF(X,Y,zFRD_3);

```

```
% [P_zFRD4,zFRD4]=denoisingcloudF(X,Y,zFRD_4);

%%

%original painting print

% figure

% pcshow(pC_zG_1);

% hold on

% pcshow(pC_zG_2);

% title('Gyroid');

figure

pcshow(pC_zSD_1);

hold on

pcshow(pC_zSD_2);

title('S-Diamond');

pcshow(pC_zSD_1);

xlabel('x');

ylabel('y');

figure
```

```
pcshow(pC_zSD_2);

xlabel('x');

ylabel('y');

% figure

% pcshow(pC_zP_1);

% hold on

% pcshow(pC_zP_2);

% title('Primitive');

figure

pcshow(pC_zFRD_1);

hold on

pcshow(pC_zFRD_2);

hold on

pcshow(pC_zFRD_3);

hold on

pcshow(pC_zFRD_4);

title('F-RD');

% %%denoising figure
```

```
% figure  
  
% pcshow(P_zG1);  
  
% hold on  
  
% pcshow(P_zG2);  
  
%  
  
% figure  
  
% pcshow(P_zSD1);  
  
% hold on  
  
% pcshow(P_zSD2);  
  
%  
  
% figure  
  
% pcshow(P_zP1);  
  
% hold on  
  
% pcshow(P_zP2);  
  
%  
  
% figure  
  
% pcshow(P_zFRD1);  
  
% hold on  
  
% pcshow(P_zFRD2);  
  
% hold on
```

```

% pcshow(P_zFRD3);

% hold on

% pcshow(P_zFRD4);

%%

%Solution of z_functions of Transitions

e=exp(1);%definition of variable 'e'

%definition of shape function

G1=('x');

G2=('x^2+y^2-(pi^2/4)');

%no solution of sphere for any couple in this theory.

for i=1:2

    eval(['Zt_G_P',num2str(i),'=transitionalF(F_G,F_P,"2",G',num2str(i),');']);

end

for i=1:2

    eval(['Zt_G_SD',num2str(i),'=transitionalF(F_G,F_SD,"2",G',num2str(i),');']);

end

for i=1:2

    eval(['Zt_P_SD',num2str(i),'=transitionalF(F_P,F_SD,"2",G',num2str(i),');']);

end

for i=1:2

```

```

eval(['Zt_G_FRD',num2str(i),'=transitionalF(F_G,F_FRD,"2",G,num2str(i),');']);
end

for i=1:2

    eval(['Zt_P_FRD',num2str(i),'=transitionalF(F_P,F_FRD,"2",G,num2str(i),');']);
end

for i=1:2

    eval(['Zt_SD_FRD',num2str(i),'=transitionalF(F_SD,F_FRD,"2",G,num2str(i),');']);
end

%%

%Pretreatment of z-function: sym-char &then put '.' before '*' & '/'

for i=1:2

    eval(['Zt_G_P',num2str(i),'_1=vectorize(char('Zt_G_P',num2str(i),'(1)));']);
    eval(['Zt_G_P',num2str(i),'_2=vectorize(char('Zt_G_P',num2str(i),'(2)));']);

    eval(['Zt_G_SD',num2str(i),'_1=vectorize(char('Zt_G_SD',num2str(i),'(1)));']);
    eval(['Zt_G_SD',num2str(i),'_2=vectorize(char('Zt_G_SD',num2str(i),'(2)));']);

    eval(['Zt_P_SD',num2str(i),'_1=vectorize(char('Zt_P_SD',num2str(i),'(1)));']);
    eval(['Zt_P_SD',num2str(i),'_2=vectorize(char('Zt_P_SD',num2str(i),'(2)));']);

```

```

% eval(['Zt_G_FRD',num2str(i),'_1=vectorize(char('Zt_G_FRD',num2str(i),'(1)));']);
% eval(['Zt_G_FRD',num2str(i),'_2=vectorize(char('Zt_G_FRD',num2str(i),'(2)));']);

eval(['Zt_P_FRD',num2str(i),'_1=vectorize(char('Zt_P_FRD',num2str(i),'(1)));']);
eval(['Zt_P_FRD',num2str(i),'_2=vectorize(char('Zt_P_FRD',num2str(i),'(2)));']);
eval(['Zt_P_FRD',num2str(i),'_3=vectorize(char('Zt_P_FRD',num2str(i),'(3)));']);
eval(['Zt_P_FRD',num2str(i),'_4=vectorize(char('Zt_P_FRD',num2str(i),'(4)));']);

% eval(['Zt_SD_FRD',num2str(i),'_1=vectorize(char('Zt_SD_FRD',num2str(i),'(1)));']);
% eval(['Zt_SD_FRD',num2str(i),'_2=vectorize(char('Zt_SD_FRD',num2str(i),'(2)));']);

end

%%

%Point cloud of transitions

[X,Y] = meshgrid(-6:0.005:6,-6:0.005:6);

x=pi./6.*X;y=pi./6.*Y;

eval(['ZtGP1_1=6./pi.*real('Zt_G_P1_1,');']);
eval(['ZtGP1_2=6./pi.*real('Zt_G_P1_2,');']);

eval(['ZtGP2_1=6./pi.*real('Zt_G_P2_1,');']);
eval(['ZtGP2_2=6./pi.*real('Zt_G_P2_2,');']);

eval(['ZtGSD1_1=6./pi.*real('Zt_G_SD1_1,');']);

```

```

eval(['ZtGSD1_2=6./pi.*real(',Zt_G_SD1_2,');']);

eval(['ZtGSD2_1=6./pi.*real(',Zt_G_SD2_1,');']);

eval(['ZtGSD2_2=6./pi.*real(',Zt_G_SD2_2,');']);

eval(['ZtPSD1_1=6./pi.*real(',Zt_P_SD1_1,');']);

eval(['ZtPSD1_2=6./pi.*real(',Zt_P_SD1_2,');']);

eval(['ZtPSD2_1=6./pi.*real(',Zt_P_SD2_1,');']);

eval(['ZtPSD2_2=6./pi.*real(',Zt_P_SD2_2,');']);

% eval(['ZtGFRD1_1=real(',Zt_G_FRD1_1,');']);

% eval(['ZtGFRD1_2=real(',Zt_G_FRD1_2,');']);

% eval(['ZtGFRD2_1=real(',Zt_G_FRD2_1,');']);

% eval(['ZtGFRD2_2=real(',Zt_G_FRD2_2,');']);

% eval(['ZtSDFRD1_1=real(',Zt_SD_FRD1_1,');']);

% eval(['ZtSDFRD1_2=real(',Zt_SD_FRD1_2,');']);

% eval(['ZtSDFRD2_1=real(',Zt_SD_FRD2_1,');']);

% eval(['ZtSDFRD2_2=real(',Zt_SD_FRD2_2,');']);

eval(['ZtPFRD1_1=real(',Zt_P_FRD1_1,');']);

eval(['ZtPFRD1_2=real(',Zt_P_FRD1_2,');']);

eval(['ZtPFRD1_3=real(',Zt_P_FRD1_3,');']);

eval(['ZtPFRD1_4=real(',Zt_P_FRD1_4,');']);

eval(['ZtPFRD2_1=real(',Zt_P_FRD2_1,');']);

```

```

eval(['ZtPFRD2_2=real('Zt_P_FRD2_2,');']);
eval(['ZtPFRD2_3=real('Zt_P_FRD2_3,');']);
eval(['ZtPFRD2_4=real('Zt_P_FRD2_4,');']);

%%

pC_ZtGP1_1=PointCloud(pCloudF(X,Y,ZtGP1_1));
pC_ZtGP1_2=PointCloud(pCloudF(X,Y,ZtGP1_2));

pC_ZtGP2_1=PointCloud(pCloudF(X,Y,ZtGP2_1));
pC_ZtGP2_2=PointCloud(pCloudF(X,Y,ZtGP2_2));

pC_ZtGSD1_1=PointCloud(pCloudF(X,Y,ZtGSD1_1));
pC_ZtGSD1_2=PointCloud(pCloudF(X,Y,ZtGSD1_2));

pC_ZtGSD2_1=PointCloud(pCloudF(X,Y,ZtGSD2_1));
pC_ZtGSD2_2=PointCloud(pCloudF(X,Y,ZtGSD2_2));

pC_ZtPSD1_1=PointCloud(pCloudF(X,Y,ZtPSD1_1));
pC_ZtPSD1_2=PointCloud(pCloudF(X,Y,ZtPSD1_2));

pC_ZtPSD2_1=PointCloud(pCloudF(X,Y,ZtPSD2_1));

```

```
pC_ZtPSD2_2=pointCloud(pCloudF(X,Y,ZtPSD2_2));  
  
pC_ZtPFRD1_1=pointCloud(pCloudF(X,Y,ZtPFRD1_1));  
  
pC_ZtPFRD1_2=pointCloud(pCloudF(X,Y,ZtPFRD1_2));  
  
pC_ZtPFRD1_3=pointCloud(pCloudF(X,Y,ZtPFRD1_3));  
  
pC_ZtPFRD1_4=pointCloud(pCloudF(X,Y,ZtPFRD1_4));  
  
  
pC_ZtPFRD2_1=pointCloud(pCloudF(X,Y,ZtPFRD2_1));  
  
pC_ZtPFRD2_2=pointCloud(pCloudF(X,Y,ZtPFRD2_2));  
  
pC_ZtPFRD2_3=pointCloud(pCloudF(X,Y,ZtPFRD2_3));  
  
pC_ZtPFRD2_4=pointCloud(pCloudF(X,Y,ZtPFRD2_4));  
  
%%  
  
figure  
  
pcshow(pC_ZtGP1_1);  
  
hold on  
  
pcshow(pC_ZtGP1_2);  
  
title('GP1');  
  
  
figure  
  
pcshow(pC_ZtGP2_1);
```

```
hold on  
  
pcshow(pC_ZtGP2_2);  
  
title('GP2');  
  
figure  
  
pcshow(pC_ZtGSD1_1);  
  
hold on  
  
pcshow(pC_ZtGSD1_2);  
  
title('GSD1');  
  
figure  
  
pcshow(pC_ZtGSD2_1);  
  
hold on  
  
pcshow(pC_ZtGSD2_2);  
  
title('GSD2');  
  
figure  
  
pcshow(pC_ZtPSD1_1);  
  
hold on  
  
pcshow(pC_ZtPSD1_2);
```

```
title('PSD1');

figure

pcshow(pC_ZtPSD2_1);

hold on

pcshow(pC_ZtPSD2_2);

title('PSD2');

figure

pcshow(pC_ZtPFRD1_1);

hold on

pcshow(pC_ZtPFRD1_2);

hold on

pcshow(pC_ZtPFRD1_3);

hold on

pcshow(pC_ZtPFRD1_4);

title('PFRD1');

figure

pcshow(pC_ZtPFRD2_1);
```

```
hold on  
  
pcshow(pC_ZtPFRD2_2);  
  
hold on  
  
pcshow(pC_ZtPFRD2_3);  
  
hold on  
  
pcshow(pC_ZtPFRD2_4);  
  
title('PFRD2');
```

Code name: denoisingF language: Matlab

```
function re=denoising(X,Y,complexZ)  
  
complexZ=complexZ(:);%Convert the matrix into a column  
  
X=X(:);%Convert the matrix into a column  
  
Y=Y(:);%Convert the matrix into a column  
  
realZ=real(complexZ);%real part  
  
absZ=abs(complexZ);%Modulus length of complexZ  
  
absrealZ=abs(realZ);%Modulus length of realpart  
  
[row,~]=find(absrealZ~=absZ);%Finds rows in which only imaginary parts exist in complexZ  
  
realZ(row,:)=[];%Removes rows with only imaginary parts  
  
X(row,:)=[];%Removes rows with only imaginary parts
```

```

Y(row,:)=[];%Removes rows with only imaginary parts

re=[X,Y,realZ];%assembly

end

```

Code name: LatticeF language: Matlab

```

function re=denoising(X,Y,complexZ)

complexZ=complexZ(:);%Convert the matrix into a column

X=X(:);%Convert the matrix into a column

Y=Y(:);%Convert the matrix into a column

realZ=real(complexZ);%real part

absZ=abs(complexZ);%Modulus length of complexZ

absrealZ=abs(realZ);%Modulus length of realpart

[row,~]=find(absrealZ~=absZ);%Finds rows in which only imaginary parts exist in complexZ

realZ(row,:)=[];%Removes rows with only imaginary parts

X(row,:)=[];%Removes rows with only imaginary parts

Y(row,:)=[];%Removes rows with only imaginary parts

re=[X,Y,realZ];%assembly

end

```

Code name: pCloudF language: Matlab

```
function P=pCloudF(X,Y,z)
```

```
[m,n]=size(z);
```

```
P=zeros(m*n,3);
```

```
for i=1:m
```

```
    for j=1:n
```

```
        r=(i-1)*n+j;
```

```
        P(r,1)=X(i,j);
```

```
        P(r,2)=Y(i,j);
```

```
        P(r,3)=z(i,j);
```

```
    end
```

```
end
```

Code name: transitionalF language: Matlab

```
function r=transitionalF(F1,F2,k,G)
```

```
gama1=['1/(1+e^((',k,')*(',G,')))'];
```

```
F=['(',gama1,')*(',F1,')+(1-',gama1,')*(',F2,')'];
```

```
r=LatticeF(F);
```